Materials & Design 252 (2025) 113785

Contents lists available at ScienceDirect

Materials & Design

journal homepage: www.elsevier.com/locate/matdes

Modeling plastic deformation of TWIP steel using cohesive zone and crystal plasticity finite element

Wang Cai [a,b,d], Chaoyang Sun [a,b,*], Hongjia Zhang [c], Lingyun Qian [a,b], Linghui Meng [a,b], M.W. Fu [d,*]

[a] School of Mechanical Engineering, University of Science and Technology Beijing, Beijing 100083, PR China
[b] Beijing Key Laboratory of Lightweight Metal Forming, Beijing 100083, PR China
[c] National Key Laboratory of Equipment State Sensing and Smart Support, College of Intelligence Science and Technology, National University of Defense Technology, Changsha 410073, PR China
[d] Department of Mechanical Engineering, Research Institute for Advanced Manufacturing, The Hong Kong Polytechnic University, Hung Hom, Kowloon, Hong Kong, PR China

ARTICLE INFO

Keywords:
Crystal plasticity
Fine and ultrafine grain
Cohesive zone model
Geometrically necessary dislocation density
TWIP steel

ABSTRACT

In this research, the cohesive zone model-crystal plasticity finite element (CZM-CPFE) method was applied to reveal the influence mechanism of grain boundaries (GBs) and grains on the mechanical properties of fine/ultrafine grained TWIP steels. The reliability and efficiency of this method were verified via corroborating with in-situ SEM tensile tests and EBSD/TEM characterisation. When the average grain size was refined from 8.49 to 0.70 μm, the yield stress increased from 181 to 317 MPa and the ultimate tensile strength from 868 to 1004 MPa with little loss of UE, which was successfully predicted by the CZM-CPFE method. Also, the neighbouring grain model revealed that stress concentrations are pronounced near GBs with high misorientation angle due to the dislocation motion and twin growth hindered by GBs. Furthermore, the simulation and experimental results indicated that the critical resolved shear stress (CRSS) for twinning increased to 202 MPa for average grain size reduction to 0.70 μm, which was much higher than the 138.5 MPa for slip, making twin activation more difficult. The application of this work in steels with moderate grain sizes can facilitate understanding of the evolution of the slip and twins and the strain hardening.

1. Introduction

Twinning-induced plasticity (TWIP) steels have the most potential as new automotive steels due to the perfect combination of their strength and ductility [1]. Nevertheless, the poor yield strength (YS) considerably limits its widespread application in critical industry fields [1]. Hence, various grain refinement enhancement strategies [2], such as equal channel angular pressing (ECAP) [3] and high-pressure torsion (HPT) [4], etc., are applied to improve the yield strength of TWIP steels [3,5,6]. However, these strategies often face the struggle of enhancing both strength and ductility [7,8]. Especially, reduced elongation after ultrafine grain (100 nm $< d <$ 1 μm) [9] refinement is a critical challenge limiting the properties enhancement of TWIP steels [10,11].

The excellent mechanical properties of TWIP steels are closely dependent on the competition and synergy between twinning and slip at the microscale [1,12–15]. Continuous formation of deformation twins dynamically reduces the mean free path (MFP) of dislocations during plastic deformation [1], which can promote strain hardening and increase strength [16]. Meanwhile, the relationship between YS and the grain size of alloys is fitted by the Hall-Petch equation [17–20]. Moreover, grain refinement elevates the stress required for twin activation [21–23], which is also regulated by the stacking fault energy (SFE) [24]. However, there is some controversy about the role of grain refinement in twinning [25]. For example, it was found that deformation twins became less frequent when $d \sim 3$ μm [21]. The nucleation number of mechanical twins was reduced when $d < 1.8$ μm [5]. Variously, when the grain size was ~ 1 μm, the source of dislocations was shifted from the grain interior to the grain boundary (GB), i.e., change of deformation mode from in-grain slip to stacking faults and deformation twin nucleation at GBs would release the elastic energy stored in the sample, which resulted in the emission of partial dislocations and effected the yielding behaviour in the early stage of deformation [10]. Also, due to the

* Corresponding authors at: School of Mechanical Engineering, University of Science and Technology Beijing, Beijing 100083, PR China (C. Sun).
E-mail addresses: suncy@ustb.edu.cn (C. Sun), mmmwfu@polyu.edu.hk (M.W. Fu).

https://doi.org/10.1016/j.matdes.2025.113785
Received 9 September 2024; Received in revised form 28 February 2025; Accepted 28 February 2025
Available online 1 March 2025

scarcity of free dislocations, a decrease in the area fraction of deformation twins was measured, while the number was increased at $d = 0.79$ μm [26]. The effects of grain size on twinning and detwinning indicated an increase in twinning for nanocrystalline face-centred cubic (FCC) metals [25]. Therefore, an in-depth exploration of twin nucleation and evolution regulated by the grain size is necessary. The influence of GBs on slip and twinning becomes more pronounced with decreasing grain size [7], which further influences the strain hardening stages [11]. Hence, numerical modelling considering both grain interior (including slip and twinning) and GBs is essential and urgent for a systematic insight into the microstructure evolution and plastic deformation mechanisms.

The reduction in grain size presents difficulties in exploring the effect of GBs on slip and twinning. However, TWIP steels have now been characterised in detail from coarse to ultrafine grain scales by electron backscatter diffraction (EBSD) and transmission electron microscopy (TEM) [3,6,10,15,27]. For instance, the critical average grain size of < 1 μm for the transition of the deformation mechanism for Fe-17Mn steels was found by the EBSD characterisation method [27]. Advanced TEM characterisation results indicated that the variation of deformation mechanisms is intimately related to discontinuous yielding behaviour due to the dislocation density controlled by mobile dislocations near the macroscopic yield point in ultrafine-grained TWIP steels [10]. The microstructure evolution of fine- or ultrafine-grained TWIP steels has displayed that the suppression of twinning by grain refinement was related to the promotion of cross-slip of dislocations and the weakening of interactions between partial dislocations [6]. Although experimental characterisation methods have exhibited significant advantages in monitoring the microstructure evolution, there are great difficulties in the quantification of many influencing factors [13]. Accordingly, numerical modelling can provide a vital approach for the exploration of fine- and ultrafine-grained materials [28–30]. The influences of grain morphology and size on the yielding mechanism [28] and grain misorientation on local deformation [29] were considered in the crystal plasticity finite element (CPFE) model. Also, a multiscale strategy for computational homogenization of polycrystalline aggregates is implemented for the analysis of the FCC polycrystal flow stresses [30]. The CPFE method is widely utilized for the quantitative analysis of plastic deformation and microstructure properties prediction [8,28,31,32]. In particular, the CPFE method considering slip, twinning and GBs provides a new approach to understanding the microstructure evolution and mechanical properties of different alloys at various grain scales [13,33,34]. Also, the accurate prediction of deformation behaviours is therefore crucial for exploring the mechanical properties of fine and ultrafine grain scales.

In finite elements, the modelling of GBs is a challenge of great interest in materials engineering. A layer of elements with thickness separated at the grain edges can be defined as GBs, but this approach is controversial for the determination of the GB thickness [35]. Voronoi polycrystalline models usually have irregular polyhedral structures [36] and it is remarkably difficult to embed GBs manually. Indeed, GBs with a few nanometres thickness can be neglected compared to micrometre scale grains. Therefore, cohesive element embedding is achieved by replicating shared nodes of neighbouring grains and then constructing nodes with zero thickness in space, which is a widely accepted GB modelling strategy [13,34,37–40]. The GBs assigned to the cohesive zone model (CZM) are usually combined with the grain interior of the CPFE model to simulate intergranular interactions [13]. Li et al. [37] predicted intergranular cracking in titanium alloys at elevated temperatures based on the CZM of GBs. In addition, Alabort et al. [34] revealed the GB properties based on experiments and the CZM-CPFE approach. Thus, the combination of the CZM and CPFE methods can provide a strategy for modelling GBs and grains, thereby deepening the comprehension of the underlying deformation mechanisms.

Furthermore, the effects of deformation mechanisms on strain hardening require specific quantitative models to illustrate [41]. Recently, CPFE and molecular dynamics simulations were developed based on the synergetic facilitation between slip, twinning and GBs [13,41,42]. Specifically, molecular dynamics was employed to simulate the formation of twins in nanocrystalline [42]. Besides, the length-scale dependence of various slip systems interactions was considered in the classical CPFE model to predict the YS and strain hardening with different grain sizes [29]. Still, the slip interactions between neighbouring grains needed an in-depth understanding [32]. Although atomic models can provide very valuable insights into the grain boundary /dislocation interactions [43,44], it is challenging to describe grain scale effects during plastic deformation [45] as modelling is usually limited by atomic number and computational cost. Furthermore, local stress monitoring of twins based on in-situ tests and high-resolution electron backscatter diffraction (HR-EBSD) suggested that the evolution of twin boundaries (TBs) was a dynamic process and that the negative shear stress during the twin propagation might be related to the stress reversal [46]. Therefore, identifying the evolution of slip and twinning is essential for performing simulations to elucidate the stress and strain distributions in the grain that they affect.

Deformation in the grain interior induces the proliferation of geometrically necessary dislocation (GND), and GND density continues to elevate with increasing strain [47]. It can be estimated based on Ashby's model [48]. The relevant equation is given by the following:

$$\rho_{GND} \cong \frac{\varepsilon_p}{4bd} \tag{1}$$

where ρ_{GND} is the density of GND. ε_p is the macro-scaled plastic strain. b denotes the magnitude of the Burgers vector. It was found that ρ_{GND} is inversely proportional to the average grain size. Zhu et al. [49] analysed the GND density of nickel during quasi-static deformation varying linearly with the plastic strain in the strain of $0.05 \sim 0.46$ using Ashby's model. In addition, the evolution of the GND density of Fe-22Mn-0.6C TWIP steel was explored by a modified Ashby's model considering the effect of twins on the MFP of dislocations [47]. The evaluation of GND density based on Ashby's model can further analyse the correlation between twinning and dislocation during strain hardening.

Based on the above studies of relevant experimental characterisation and numerical modelling, the main objective of the present research is to explore the mechanical properties and plastic deformation behaviours of TWIP steels affected by grain size, which combines the CPFE method for slip and twinning and the CZM for GBs. Considering the thickness relationship of grain and GB and the feasibility of modelling, the thickness of the GB can be considered as zero. Therefore, the zero-thickness GB is constructed [13,34] while considering the dislocation density. Sheets with average grain sizes ranging from 0.70 to 8.49 μm were obtained by combining three passes of cold rolling and annealing processes, and the microstructure evolution is observed by the EBSD/TEM characterisation of specimens after prestrain and in-situ SEM tensile experiments. Then, the reliability of the CZM-CPFE method considering GBs can be validated by the experimental results in terms of mechanical responses, plastic deformation behaviours and microstructural evolutions. Finally, the effects of misorientation angle on mechanical properties of neighbouring grains and activation of slip and twinning on strain hardening are analysed using simulations and EBSD/TEM characterization. Furthermore, the GND density is estimated using the modified Ashby's model, which takes into account the evolution of dislocations and twins. This work can deepen the understanding of the plastic deformation mechanisms and provide essential insights into the application of crystal plasticity at fine and ultrafine grain scales.

2. CZM-CPFE method considering GBs

2.1. Continuum-based kinematics

Based on prior expressions [12,13], the deformation gradient tensor is usually given by: $\mathbf{F} = \mathbf{F}^e\mathbf{F}^p$. $\mathbf{F}^e$ is the elastic tensor and $\mathbf{F}^p$ is the plastic

tensor [50,51]. The constitutive equation is expressed by: $\mathbf{T}^{e} = \mathfrak{R} : \mathbf{E}^{e}$, where $\mathfrak{R}$ is an elasticity tensor consisting of C_{11}, C_{12} and C_{44}. $\mathbf{T}^{e}$ is the second Piola-Kirchoff (PK) stress tensor. $\mathbf{E}^{e}$ is the Green-Lagrange strain tensor, which is calculated by: $\mathbf{E}^{e} = \left(\mathbf{F}^{eT}\cdot\mathbf{F}^{e} - \mathbf{I}\right)/2$. $\mathbf{T}^{e} = (\det\mathbf{F}^{e})\mathbf{F}^{e-1}\boldsymbol{\sigma}\mathbf{F}^{e-T}$, where $\boldsymbol{\sigma}$ is the symmetric Cauchy stress tensor. The superscript T and –T denote the matrix transpose and the inverse of the transpose matrix, respectively. The plastic deformation velocity gradient tensor $\mathbf{L}$ can be divided into the elastic part $\mathbf{L}^{e}$ and the plastic part $\mathbf{L}^{p}$, which can be represented as:

$$\mathbf{L}=\dot{\mathbf{F}}\cdot\mathbf{F}^{-1}=\dot{\mathbf{F}}^{e}\cdot\mathbf{F}^{e-1}+\mathbf{F}^{e}\dot{\mathbf{F}}^{p}\cdot\mathbf{F}^{p^{-1}}\cdot\mathbf{F}^{e^{-1}} = \mathbf{L}^{e}+\mathbf{L}^{p} \quad (2)$$

where $\mathbf{L}^{p}$ can be considered by two parts: slip and twinning [50,51]. The slip in twin lamellae is not included because of the thin thickness and low proportion of twins in the experimental steels. Therefore, $\mathbf{L}^{p}$ is described by the following:

$$\mathbf{L}^{p} = (1-f_t)\sum_{\alpha=1}^{12}\dot{\gamma}^{\alpha}(\mathbf{m}^{\alpha}\otimes\mathbf{n}^{\alpha}) + \sum_{\beta=1}^{12}\dot{\gamma}^{\beta}(\mathbf{m}^{\beta}\otimes\mathbf{n}^{\beta}) \quad (3)$$

where $\dot{\gamma}^{\alpha}$ and $\dot{\gamma}^{\beta}$ are the individual shear strain rates for the slip and twin systems. $\mathbf{m}^{\alpha}$ and $\mathbf{n}^{\alpha}$ are the unit vectors along the shear and normal directions in the slip plane, while $\mathbf{m}^{\beta}$ and $\mathbf{n}^{\beta}$ are those of the twinning plane. $\otimes$ denotes the tensor product. f_t is the total twin volume fraction, which is calculated by: $f_t = \sum_{\beta=1}^{12} f^{\beta}$, where f^{β} is the twin volume fraction of the individual twin system. If f_t achieves the critical value f_0, the initial grain orientation is rotated to its mirror image along the $\{111\}-$type twinning plane [12,14]. The rotation matrix $\mathbf{R}$ between the twin parent and variant is given by the following:

$$\mathbf{R} = 2\mathbf{n}^{\beta}\otimes\mathbf{n}^{\beta} - \mathbf{I} \quad (4)$$

where $\mathbf{I}$ is the unit tensor.

The accumulated shear strains of slip (Γ^{slip}) and twinning (Γ^{twin}) can describe the contributions of slip and twinning to plastic strain [44]. They are calculated by the following:

$$\Gamma^{slip} = \int_0^t \sum_{\alpha=1}^{N}\Gamma^{twin} = \int_0^t \sum_{\beta=1}^{N}|\dot{\gamma}^{\alpha}|dt, |\dot{\gamma}^{\beta}|dt \quad (5)$$

Furthermore, classical crystal plasticity is frequently used for the plastic deformation behaviour of grains without considering the damage behaviour induced by strain localization [52,53]. Plastic deformation is derived from the accumulated effects of microscopic slip and twinning [54]. Damage initiation is often intimately related to the local equivalent plastic strain [44]. In this work, the damage factor D_G can be defined by the following:

$$D_G = \int \frac{d\varepsilon_{eq}}{\varepsilon_f} \quad (6)$$

where ε_f is the fracture strain. ε_{eq} denotes the equivalent plastic strain. The initial $D_G = 0$ implies there is no damage. As the D_G gradually increases to 1, indicating that the grain is progressively damaged to fracture.

2.2. Crystal plasticity of slip and deformation twinning

2.2.1. Kinetic description of slip

Based on the classical Orowan equation [55], the $\dot{\gamma}^{\alpha}$ using dislocation density as a state variable in Eq. (3) are commonly given by the following:

$$\dot{\gamma}^{\alpha} = \rho^{\alpha}bv_0\exp\left\{-\frac{Q_s}{k_BT}\left[1-\left(\frac{\left|\tau^{\alpha}_{eff}\right|}{\tau_l+\tau_{sol}}\right)^{p}\right]^{q}\right\}\mathrm{sign}(\tau^{\alpha}) \quad (7)$$

where ρ^{α}: the dislocation density of the slip system α, b: the magnitude of Burgers vector for perfect dislocation, v_0: the reference movement velocity of dislocation, Q_s: the activation energy of dislocation, k_B: the Boltzmann constant, T: the absolute temperature. p and q are the exponents of the slip velocity. τ^{α} and τ^{α}_{eff} are the resolved shear stress (RSS) and the effective RSS of the slip system α. τ_l and τ_{sol} are the lattice friction and solid solution stress, respectively.

τ^{α}_{eff} can be represented by τ^{α} and the stress τ^{α}_{p} [56]:

$$\tau^{\alpha}_{eff} = \begin{cases}\tau^{\alpha}-\tau^{\alpha}_{p} & if\,\tau^{\alpha}\geq\tau^{\alpha}_{p}\\ 0 & if\,\tau^{\alpha}<\tau^{\alpha}_{p}\end{cases} \quad (8)$$

For TWIP steels, considering the obstacles of forest dislocations and the effect of GBs, the stress is given by the following [23]:

$$\tau^{\alpha}_{p} = \tau^{\alpha}_{0}+\frac{K_{hp}}{\sqrt{d}}+Gb\sqrt{\sum_{\alpha'=1}^{12}A_{\alpha\alpha'}\rho^{\alpha'}} \quad (9)$$

where τ^{α}_{0} is the initial resistance when grain size d is quite large [56]. G is the shear module. K_{hp} denotes the Hall-Petch slope. $A_{\alpha\alpha'}$ is the interaction matrix between the slip systems α and α', involving self-hardening (A_0), coplanar (A_1), co-linear (A_2), orthogonal (A_3), glissile (A_4) and sessile (A_5) types [57] in A ppendix A. $\rho^{\alpha'}$ is the dislocation density of the slip system α'.

The solid solution stress τ_{sol} is given by the following [58]:

$$\tau_{sol} = \sum_{j=1}^{n}p_jM_j \quad (10)$$

where M_j and p_j are the uniformly distributed mass concentration and the inherent strengthening effect of the alloying element j. Clearly, this equation is based on the contribution of each alloy element.

Strain hardening is mainly regulated by the dislocation density [8]. The evolution of the dislocation density ρ^{α} for each slip system α is described by the following [55,59]:

$$\dot{\rho}^{\alpha} = \frac{1}{b}\left[\max\left(\frac{1}{l_{\alpha}},\frac{K_{\rho}}{d}\right)-2y_c\rho^{\alpha}\right]|\dot{\gamma}^{\alpha}| \quad (11)$$

where $\dot{\rho}^{\alpha}$ denotes the rate of dislocation accumulation, depending on the MFP of dislocations l_{α} [60,61]. y_c is proportional to the critical annihilation distance of the dislocation [62]. K_{ρ} denotes a dimensionless constant controlling the dislocation storage [30]. In addition to GBs affecting the MFP of dislocations, microstructures inside the grains should not be neglected. Thus, considering $60^{\circ}\sum 3\{111\}$ coherent TBs and the interaction between dislocations, l_{α} in Eq. (11) is given by the following:

$$\frac{1}{l_{\alpha}} = \frac{1}{d}+\frac{1}{T^{\alpha}}+\frac{\sqrt{\sum_{i\neq\alpha}\rho^{i}}}{K} \quad (12)$$

where K is a fitting parameter associated with the dislocation accumulation [63,64]. T^{β} is the spacing between the twin secant to the slip system, which is defined by the following [63]:

$$\frac{1}{T^{\alpha}} = B^{\alpha\beta}\frac{1}{d_{\beta}}, \frac{1}{d_{\beta}} = \frac{f^{\beta}}{2re(1-\sum_{\beta=1}^{12}f^{\beta})} \quad (13)$$

where d_{β} denotes the length between two twins [65]. r is the mean number of microtwins per stack. e denotes the average thickness of twins [63]. TBs' effect on dislocations is similar to that of GBs. Once the twin is activated, if the slip and twin systems are not coplanar, the twin will prevent the dislocation motion, whereas when the slip and twin systems are coplanar, the twin will not affect the dislocation. $B^{\alpha\beta}$ follows the following rule [65].

$B^{\alpha\beta} = 0$, the slip system and the twin system are coplanar.

$B^{\alpha\beta} = 1$, the slip system and the twin system are secant.

2.2.2. Deformation twinning

Shear deformation is produced parallel to the twinning plane during the twinning process. The shear strain rate $\dot{\gamma}^{\beta} = r_{tw}\dot{f}^{\beta}$, where $r_{tw} = 0.707$ for FCC-type lattice. The twin volume fraction f^{β} is the integral of $\dot{f}^{\beta}$ in a specific time period ζ, i.e. $f^{\beta} = \int_0^{\zeta_1} \dot{f}^{\beta}(\zeta)d\zeta, \dot{f}^{\beta}$, can be calculated by the following [60]:

$$\dot{f}^{\beta} = (1 - f_t)V^{\beta}\dot{N}_{tw}^{\beta} \tag{14}$$

where $\dot{N}_{tw}^{\beta}$ is the twin nucleation rate. V^{β} is the volume of a new twin, which is defined by the following:

$$V^{\beta} = \frac{\pi}{4}edl_{\beta}, \frac{1}{l_{\beta}} = \frac{1}{d} + \frac{1}{T^{\beta}} \tag{15}$$

where l_{β} is the average spacing between two barriers. e is the average thickness of twins. In this work, T^{β} and T^{α} are equal due to the capability of the boundary to prevent the twin growth. Also, the generated twin is considered disc-shaped.

$\dot{N}_{tw}^{\beta}$ is influenced by many factors, such as cross-slip and RSS for twinning. The RSS is intimately related to the twin activation. Furthermore, partial dislocation reactions and local stress can also affect twin nucleation [60]. However, the effect of cross-slip can reduce dislocation piled up to relieve local stress and weaken the interaction between partial dislocations. Thus, $\dot{N}_{tw}^{\beta}$ can be given by the following:

$$\dot{N}_{tw}^{\beta} = \dot{N}_0 \tag{16}$$

where $\dot{N}_0$ is the density of the potential twin nucleation rate. p_{tw} is the probability of the stacking faults bending to form a twin lamella [60,66]. p_{cs} is the probability of a cross-slip event occurring, which is given by the following:

$$p_{cs} = \exp\left[-\frac{V_{cs}}{k_B T}(\tau_r - \tau^{\beta})\right] \tag{17}$$

where τ^{β} is the RSS for twinning. V_{cs} is the activation area of a cross-slip event. τ_r is the required stress to reduce the critical distance x_c between two partial dislocations from the equilibrium distance x_0 to promote twin nucleation without the externally applied stress [60], which can be calculated by the following:

$$\tau_r = \frac{Gb}{2\pi(x_0 + x_c)} + \frac{Gb}{4\pi x_0} \tag{18}$$

where the critical distance $x_c = 1$ nm is often set [60]. The equilibrium distance x_0 is determined by the following:

$$x_0 = \frac{Gb^2}{8\pi\gamma_{SFE}}\frac{2+\nu}{1-\nu} \tag{19}$$

where γ_{SFE} represents the value of the SFE. ν denotes the Poisson ratio.

The probability p_{tw} associated with the RSS for twinning is defined by the following:

$$p_{tw} = \exp\left[-\left(\frac{\tau_{twin}^{c}}{\tau^{\beta}}\right)^{s}\right] \tag{20}$$

where s is the fitted model parameter, which is determined by the transition degree of the non-twinning to the twinning stress domain [60]. τ_{twin}^{c} is the critical resolved shear stress (CRSS) for twin formation, which can be obtained by using many methods [21,60,67,68]. Based on the twin nucleation mainly near GBs [21] and the shear stress required for twin growth [60], τ_{twin}^{c} can be given:

$$\tau_{twin}^{c} = \frac{\gamma_{SFE}}{b_p} + \frac{Gb_p}{d} \tag{21}$$

where $b_p = \sqrt{3}b/3$. γ_{SFE} is calculated by using the thermodynamic model [69]. It is noteworthy that the smaller grain size and higher SFE values make twin nucleation and growth more difficult.

2.3. Cohesive zone model for GBs

For fine- and ultrafine-grained steels, the GBs during plastic deformation is not negligible [70]. The constitutive equations based on the CZM can provide a viable basis for predicting mechanical behaviour and have been widely used [34,71]. In this research, the bilinear traction separation law (TSL) of the CZM was employed, which is mainly divided into the elastic and softening stages, where the stress is defined by the following:

$$\tau_i = (1 - D_{GB})K_i(\delta_i/T_i) \tag{22}$$

where $i = n, s$ and t, indicate the normal and two tangential directions. K_i represents the stiffness. T_i is defined as the normalized thickness for calculation [34]. D_{GB} denotes the damage indicator of GB, which is illustrated by the following:

$$D_{GB} = \begin{cases} 0 & 0 \le \delta_i < \delta_i^0 \\ \dfrac{\delta_i^f(\delta_i^m - \delta_i^0)}{\delta_i^m(\delta_i^f - \delta_i^0)} & \delta_i^0 \le \delta_i < \delta_i^f \\ 1 & \delta_i > \delta_i^f \end{cases} \tag{23}$$

where δ_i^0 is the displacement at damage initiation. δ_i^f is the displacement with the GBs cracking. δ_i^m is the maximum value of cracking. δ_i denotes the current displacement value.

When considering the GB softening stage, δ_i^m is the displacement at maximum stress and δ_i^f is the final failure displacement. They determine the damage initiation and damage evolution, respectively. The strain at the damage initiation ε_i^m can be calculated by the maximum stress τ_i^m and the stiffness K_i: $\varepsilon_i^m = \tau_i^m/K_i$. Here, the quadratic nominal stress criterion (QUADS) can be given by the following:

$$f = \left\{\frac{\langle\tau_n\rangle}{\tau_n^m}\right\}^2 + \left\{\frac{\tau_s}{\tau_s^m}\right\}^2 + \left\{\frac{\tau_t}{\tau_t^m}\right\}^2 \tag{24}$$

where τ_n, τ_s and τ_t are normal and two tangential stresses, respectively. $f = 1$ is the indication for GB entering the softening stage. Subsequently, the stage can be defined by the power law, which can be given by the following [34,72]:

$$\left\{\frac{G_n}{G_n^C}\right\}^{\lambda} + \left\{\frac{G_s}{G_s^C}\right\}^{\lambda} + \left\{\frac{G_t}{G_t^C}\right\}^{\lambda} = 1 \tag{25}$$

where G_n, G_s and G_t are the normal and two tangential energies. The fracture energy $G_i^C = \int_0^{\delta_i^f} \tau_i d\delta_i = \frac{1}{2}\cdot\tau_i^m\cdot\delta_i^f$, $i = n, s$ and t. The exponent λ can be determined by considering the contributions of each stress under mixed mode loading, i.e., the required energy for cohesive element failure in each mode.

2.4. Simulation implementation methodology

A CPFE method considering the CZM for GBs is developed to explore the plastic deformation behaviours of TWIP steels with different initial grain sizes, which not only enhances the predictive capability of the CPFE model but also an implementation methodology of the crystal plasticity is applied in the intergranular interactions. The representative volume elements (RVEs) are constructed using Neper open-source

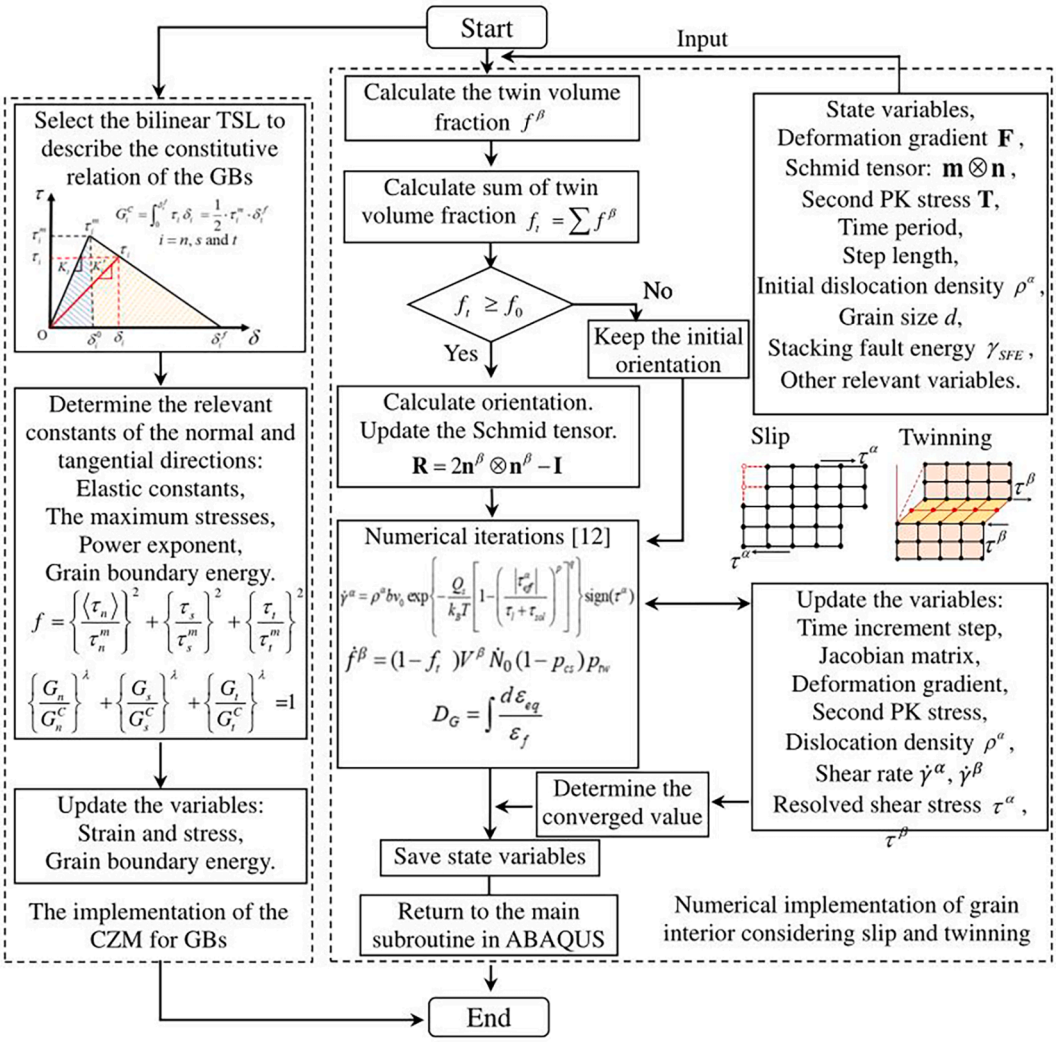

Fig. 1. The flow chart of numerical implementation in ABAQUS/Standard considering the CPFE model coupling slip and twinning [12] and the CZM for GBs.

Table 1
The final chemical composition of TWIP steel in this work (weight %).

C	Mn	Si	Al	S	P	Ti	Fe
0.59	15.68	0.074	1.19	0.006	0.008	≤0.01	Bal.

software. Then, zero-thickness GBs are inserted from between grains by using an open-source Python algorithm. The CPFE model considering twinning is developed. The ABAQUS/Standard is utilized to execute the algorithm of crystal plasticity considering slip and twinning into the user-defined materials subroutine (UMAT) and call them up in the material properties, while reading in the grain size d and other state variables. Finally, uniaxial tensile of different RVEs are simulated based on the CZM-CPFE method to analyse the contributions of GBs, slip and twinning to strain hardening and damage evolution. The flow chart of the above steps implemented based on the above methodology is shown in Fig. 1.

The numerical implementation methodology mainly includes the CPFE method for deformation twinning, slip and the CZM for GBs. The physical properties of GBs are also assigned the constitutive equations to explore their mechanical properties, based on GBs as part of a polycrystalline material solid.

Firstly, the numerical calculation of the CPFE model is mainly divided into parameter initialisation, main procedure iteration, variables update and output in the following:

(1) Read the material parameters, such as initial dislocation density, initial values of state variables, and the plastic deformation gradients.

(2) Calculate the second PK stress, Schmid tensor, the twin volume fraction f^β and obtain the sum of all twin volume fractions f_t, determine whether the conditions of grain rotation are met by comparing the threshold value f_0.

(3) Update the grain orientation and Schmid tensor, then enter the numerical iterations.

(4) Based on prior work [12], the convergence criterion is applied to update the second PK stresses and relevant state variables.

Meanwhile, the implementation methodology for modelling the CZM for GBs can be divided into two main steps in the following:

(1) Select the bilinear TSL constitutive equations suitable for analysing the mechanical properties of GBs.

(2) Determine the elastic constants, the maximum stresses and the grain boundary energies of the normal and two tangential directions, respectively.

Finally, the results can contribute to the basis for analysing the mechanical behaviours of the relevant grains and GBs.

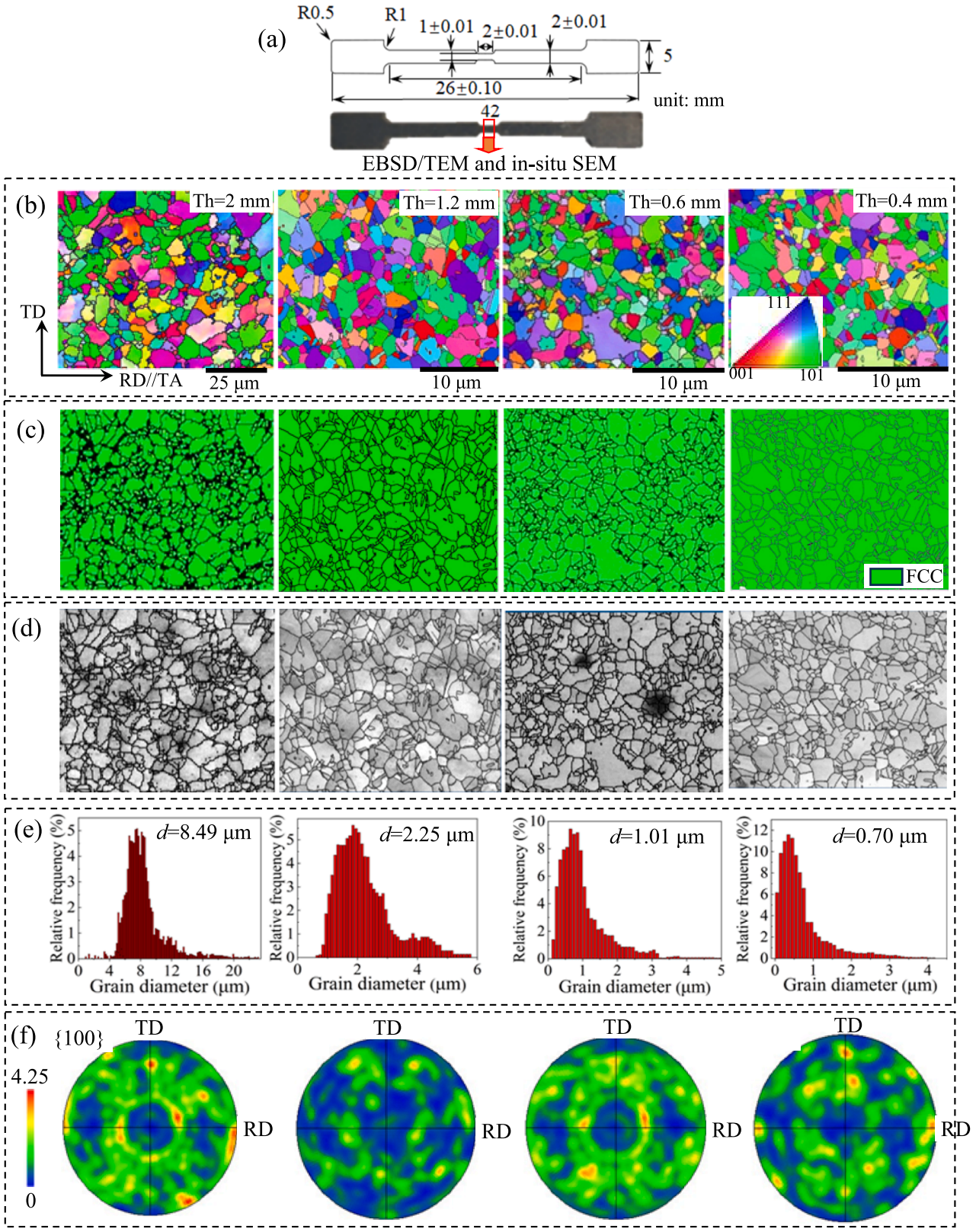

Fig. 2. TWIP steels with various grain sizes prepared by combining rolling and annealing: (a) specimen dimension; (b) the IPFs, (c) phase maps, (d) IQ maps, (e) grain size statistics and (f) the {100} PFs of these TWIP steels.

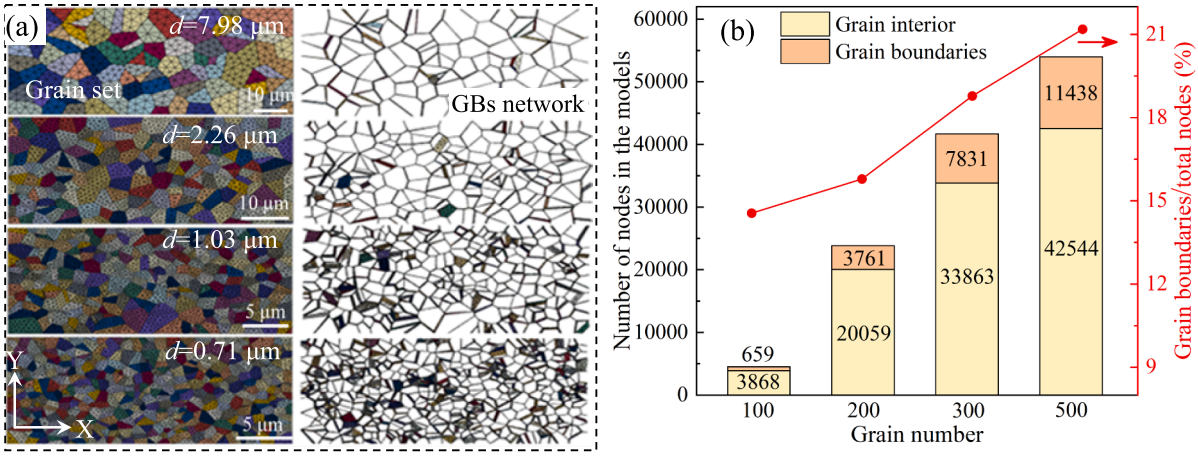

Fig. 3. Grain interior and GBs network (a) meshing by using the C3D4 and COH3D6 element types, and (b) the statistics of nodes for RVEs with different grain numbers.

Table 2
Material parameters in CPFE model simulations.

Physical meaning	Symbol	Equation number	Model inputs
Elastic constants (GPa)	C_{11}	–	198 [65]
	C_{12}	–	125 [81]
	C_{44}	–	122 [81]
Twin volume fraction threshold	f_0	–	0.3
The magnitude of the Burgers vector	b	(7)	0.25 nm
Reference velocity for dislocation	v_0	(7)	10^{-4} m/s [23]
Initial dislocation density	ρ_0^α	(7)	10^{12} m^{-2} [82]
The activation energy for slip	Q_s	(7)	1.61×10^{-19} J
The lattice friction	τ_l	(7)	3 MPa [23]
Exponents in slip velocity	p, q	(7)	$p = 1.15$; $q = 1.0$ [23]
The initial resistance on slip system α	τ_0^α	(9)	5 MPa
Annihilation distance for dislocations	y_c	(11)	1.43 nm
Dimensionless constant	K_ρ	(11)	5 [30]
The material constant	K	(12)	64
The average number of twins per stack	r	(13)	5 [65]
Mean twin thickness	e	(13)	10 nm [63]
Potential twin nucleation rate	$\dot{N}_0$	(16)	2.0×10^{15} s^{-1} [68]
The cross-slip activation volume	V_{cs}	(17)	1.67×10^{-29} m^3 [23]
The fitting parameter	s	(20)	5
Stacking fault energy	γ_{SFE}	(21)	27.8 mJ/m^2

Table 3
Constitutive parameters of the CZM for GBs.

Physical meaning	Symbol	Equation number	Model inputs
Young's modulus of GB	K_n	(22)	2100 GPa [80]
	K_s, K_t	(22)	840 GPa [78]
Damage initiation strains	ϵ_n^m,ϵ_s^m,ϵ_t^m	–	1.0×10^{-3} [78]
Maximum stresses	τ_n^m	(24)	2100 MPa
	τ_s^m,τ_t^m	(24)	$\tau_n^m/(2 \times (1+\nu))$ [79]
The power law exponent	λ	(25)	1 [72]

3. Mechanical experiments and microstructure characterization

3.1. Materials and specimen preparation

TWIP steel was melted in a protective atmosphere of Ar and the final composition is shown in Table 1. Then, it was hot rolled to prepare a 10 mm thick sheet, which was then annealed at 900 °C and cold rolled to 2 mm thickness in three passes [73]. Initial sheets with d = 8.49 μm approximately were prepared. These TWIP steel sheets were produced by controlling the different press-down displacements (0.8, 0.6 and 0.2 mm). This combined the stress relief heat treatment process at 700 °C for 10 min with a 2 mm thick sheet subjected to ≤ 1500 KN rolling stress on each side in a two-roller cold rolling mill. Four sheet thicknesses (0.4, 0.6, 1.2 and 2 mm) were finally achieved via cold rolling and annealing.

The elongated grains along the rolling direction (RD) usually had higher internal stresses, which negatively affected the microstructure observation. Therefore, the electrical resistance furnace was used to anneal the rolled sheets. A staged heating mode was adopted for the annealing process. Specifically, it was heated from room temperature to 600 °C at 10 °C/min, then to 700 °C at 3 °C/min, held for 5 min and cooled in the furnace.

The experimental tensile specimens in Fig. 2**(a)** were produced by using the slow-walking molybdenum wire electrical discharge machining (EDM). Then, the ground process was conducted on these specimens until their surfaces were flat and smooth without apparent defects, which could reduce experimental errors in subsequent mechanical properties tests due to the specimens themselves. The inverse pole figures (IPFs), phase maps and image quality (IQ) maps of the specimen gauge region with different thicknesses (Th) in Fig. 2**(a)** are displayed by using EBSD in Fig. 2**(b)-(d)**. Also, their grain sizes were statistically analysed and the calculated results are presented in Fig. 2**(e)**. These IPFs indicate that the microstructure is entirely austenite. The {100} pole figures (PFs) in Fig. 2**(f)** illustrate no apparent initial texture effect. It is found that the sheets before rolling consist essentially of fine grains, and the ones after rolling contain both fine and ultrafine grains, except that different thicknesses of the sheets have different proportions of ultrafine grains.

3.2. Experimental procedures

The polished specimens were clamped on the tensile testing machine (WDW-200), and the strain rate was set at 0.001/s. Different specimens were stretched to different strains (0.10, 0.30, 0.50 and fractured). The tension axis (TA) was parallel to the RD. The displacement variation in the specimen gauge areas was measured using an extensometer, and

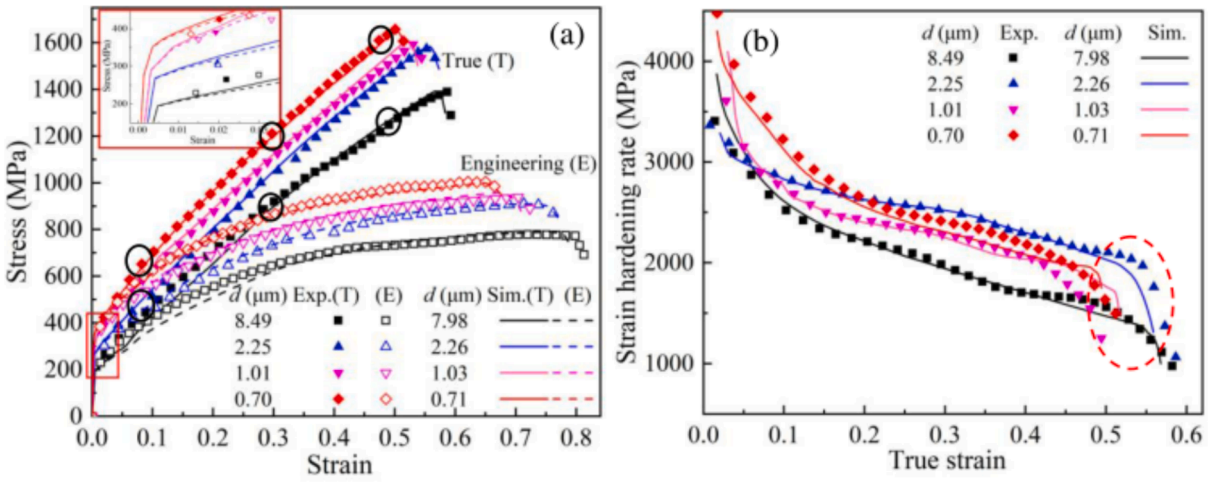

Fig. 4. Experimental and simulated results: (a) stress–strain responses and (b) strain hardening rate curves. The solid red box presents the YS and the black solid circles are the strains of 0.10, 0.30 and 0.50. The numbers in parentheses indicate the average grain sizes of RVEs.

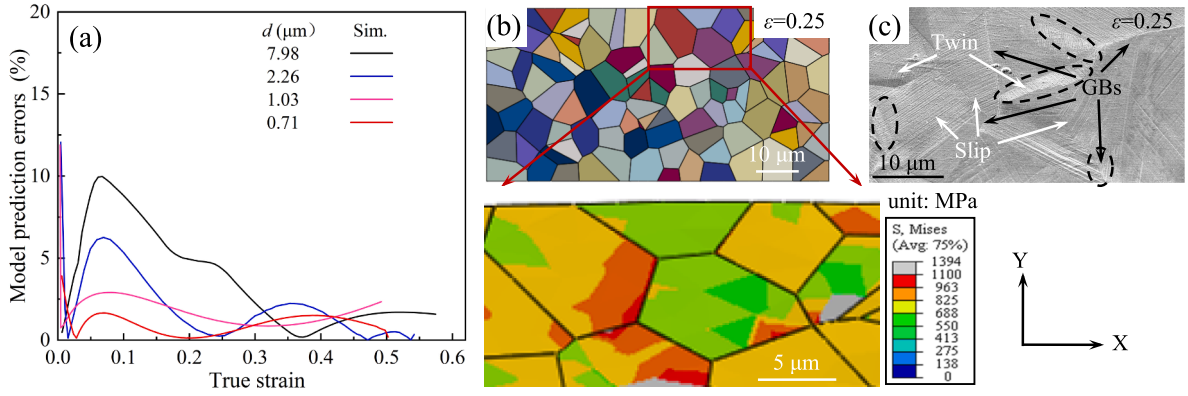

Fig. 5. Models with GBs modelled by the CZM: (a) prediction errors of true stress and (b) localized stress maps at $\varepsilon = 0.25$. (c) Microscopic morphology of the specimen at $\varepsilon = 0.25$. The black dotted lines denote the stress concentration areas in (c).

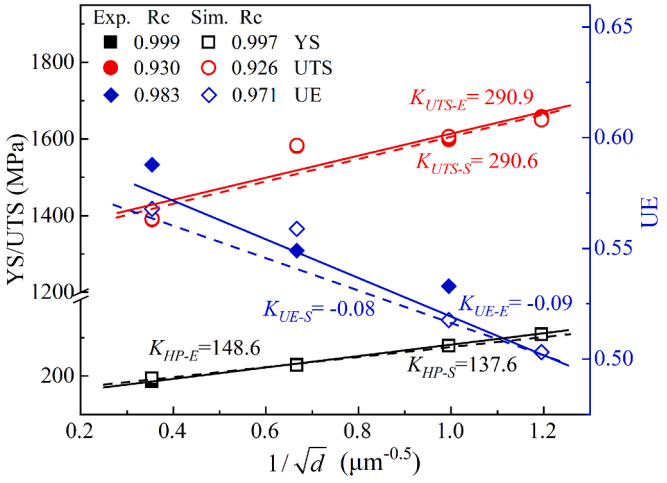

Fig. 6. Variation of the YS, UTS and UE with grain size. Rc indicates the correlation coefficient.

then the displacement of the specimen during the preloading stage was removed to calculate the engineering and true strains. To capture the microstructural information of different specimens, all specimens were polished with SiC sandpaper and diamond abrasive paste. Finally, electrochemical polishing was achieved by using an electrolyte solution consisting of 10 % perchloric acid–ethanol ($HClO_4$-C_2H_5OH) [74,75] at the voltage of 20 V in an ice-water bath for 40 ~ 60 s. The prepared specimens were detected by using a field emission scanning electron microscopy (FE-SEM 7100) equipped with an EBSD probe. As the grain size reached the fine or ultrafine grain scale, the scanning step length was set to 0.08 ~ 0.2 μm to improve the scanning efficiency. Then, the EBSD data was collected and analysed based on the HKL 5-channel software platform equipped with the TSL-EDAX EBSD system. The results are given in Fig. 2. Moreover, to obtain the microstructural evolution at different loading stages, the specimens were eroded to present the GBs distribution. The specimens were then clamped in an in-situ tensile device and tensed at a strain rate of 0.001/s, and then the morphological evolution was observed using the SEM.

Furthermore, the gauge areas of these deformed specimens were prepared as flat specimens with a thickness of about 0.5 mm using EDM. Then, they were ground to a thickness of less than 100 μm using different-sized SiC sandpaper. Then, small discs with a diameter of ~ 1 mm were fabricated in the stamping machine and ground to a thickness of less than 75 μm foil with SiC sandpapers. Finally, these discs were further thinner and perforated via electrochemical polishing using an electrolyte solution (90 % methanol and 10 % perchloric acid) at 20 V and −30 °C. Microstructural observations of the specimens were conducted using a FEI Tecnai F30 instrument operated at 200 kV to observe the dislocation pile-up near GBs and the distribution of the lamellar twins.

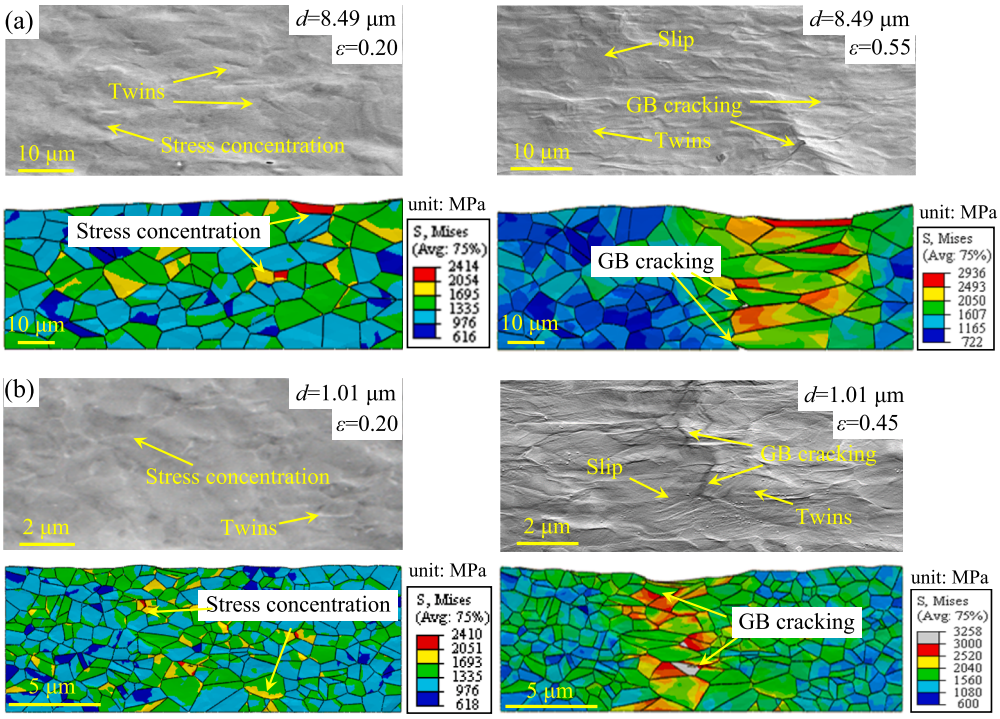

Fig. 7. Stress concentrations and GB cracks during the in-situ tensile tests and simulation results for TWIP steel with (a) d = 8.49 μm and (b) d = 1.01 μm.

4. CPFE model construction and experimental validation

4.1. RVEs with different grain sizes

Polycrystalline RVEs consisting of 100, 200, 300 and 500 randomly shaped grains (>100 grains [34]) were generated using the Voronoi algorithm in defined various size regions and the results are exhibited in Fig. 3. Their average grain sizes are 7.98, 2.26, 1.03 and 0.71 μm in Fig. 3**(a)**, respectively. This is, in general, consistent with the grain size statistics based on EBSD data in Fig. 2. Statistically, RVEs can be considered as microstructural repetitions of fine- or ultrafine-grained TWIP steels.

To ensure good refinement for improving the computational accuracy, the C3D4 (4-node linear tetrahedron) and the COH3D6 element types are chosen to adapt microstructures in Fig. 3**(a)**. Thus, these models in Fig. 3**(b)** are subdivided into 4527, 23820, 41694 and 53982 nodes, respectively, while the network structures of GBs become denser with the increase in the grain number. Due to the limitations of the equipment for the in-situ tensile experiments, the initial specimens with different thicknesses were sanded and polished to a thickness of less than 0.3 mm. Then, after electrochemical polishing, the thickness was about 0.2 μm, which is much lower than the dimensions in the observed area. The RVEs were established based on the symmetry of the X, Y and Z axes, and the thickness of the RVE was about 10 % of the width. Thus, the 3-dimensional RVEs have elements with 3 ~ 5 layers in the thickness direction (Z-axis). In addition, the fraction of GBs nodes increases from 14.5 % to 21.2 % with decreasing grain size, which is consistent with this research [76].

4.2. Calibration of RVEs parameters

To determine the parameters of the CPFE model considering slip and twinning and embedding the GBs modelled by the CZM, the present work referred to different references for the important physical variables [22,60,63]. Firstly, it is generally accepted that the twin thickness becomes thinner as the grain size decreases [1,22]. Meanwhile, the twin thickness increases with strain [23], however its evolution is difficult to present in finite element simulations. Therefore, e = 10 nm is suitable [63] and does not vary with strain for all RVEs. The contribution of twins to the plastic strain generally does not exceed 3 %, and the twin volume fraction is usually between 0.1 and 0.2 [1]. In this research, the threshold value of the twin area fraction is 0.3 in the simulations. Then, the γ_{SFE} is 27.8 mJ/m^2 determined by using the proposed model [69]. GBs are often boundary conditions for dislocation nucleation, pile up and annihilation [77]. Here, zero-thickness GBs are solid elements and thus have relevant physical properties. Based on the calibration procedures of CZM parameters in some references [37,72,78,79], the elastic stage-related parameters are firstly determined. According to the strength of GBs at room temperature is higher than that of grain interiors [80] and the methodology in this work [37], K_n = 2100 GPa, and $K_s = K_t = K_n/(2\times(1+\nu))$ = 840 GPa is selected here. The damage initiation strain $\varepsilon_n^m = \varepsilon_s^m = \varepsilon_t^m = 10^{-3}$ [78], so τ_n^m = 2100 MPa and $\tau_s^m = \tau_t^m$ = 840 MPa. Regarding the power law exponent λ = 1 is calculated in detail [72]. There are specific parameters that reflect grain size effects, including the stress following the Hall-Petch law, the evolution of dislocation density, twin area fraction and critical twinning stress. These parameters for this work are described below in Tables 2 and 3.

Several other parameters require further discussion before they are determined. Specifically, the Hall-Petch slopeK_{HP} = 148.6 MPa·μm$^{0.5}$ was fitted from the yield stress σ_Y based on the equation $\sigma_Y = \sigma_0 + K_{HP}/\sqrt{d}$. The average Schmid factor m_{slip} = 0.447 was measured in experiments so that K_{hp} is 66.4 MPa·μm$^{0.5}$ for each slip system. The shear modulus G and Poisson's ratio ν were calculated from C_{11}, C_{12} and C_{44}. The solid solution strength τ_{sol} = 55.3 MPa was calculated for typical TWIP steels with different alloying elements (wt.%) [58].

4.3. Validation of the CZM-CPFE method

4.3.1. Mechanical properties

Crystal plasticity considering slip and twinning is implemented by using the UMAT. In Fig. 3**(a)**, based on the labelling of the axes, symmetric constraints are utilized on the X-Y-Z axis (U = UR = 0), while the right boundary of the X-axis is loaded with displacement to achieve uniaxial tensile. "U" and "UR" represent the degrees of freedom for

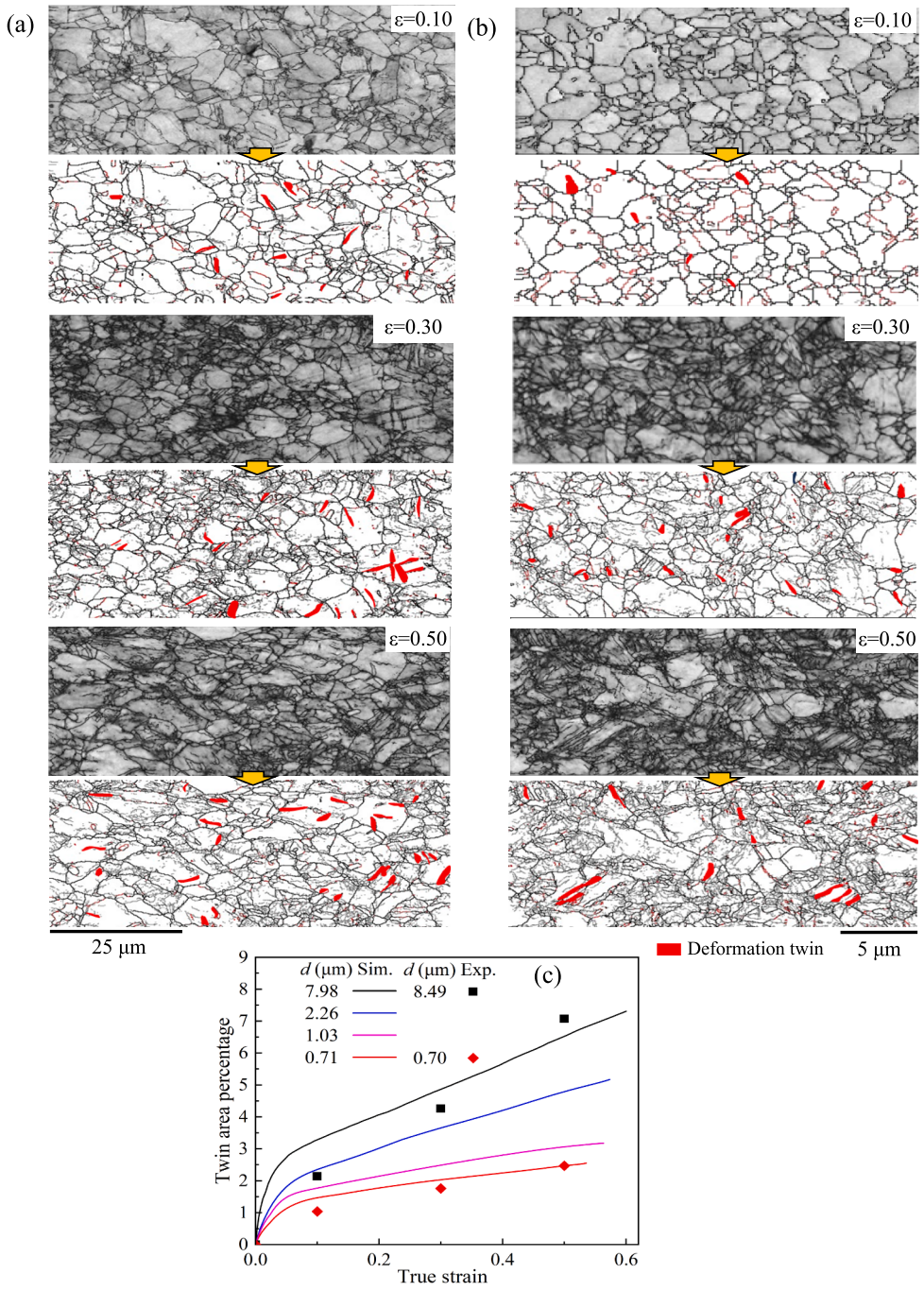

Fig. 8. Deformation twins in the IQ-GBs maps of TWIP steel with (a) $d = 8.49$ and (b) $d = 0.70$ μm. (c) Twin area fractions with true strain for RVEs and specimens with various grain sizes.

displacement and rotation, respectively. For each time step, the shear strain increments for each slip and twin system are solved using an implicit time integration algorithm [12,13] in Fig. 1. The engineering and true stress–strain relationships are consistent with the simulation results presented in Fig. 4**(a)**, confirming the reliability of the CZM-CPFE method. It is worth noting that the models can predict the strain hardening and damage evolution well. Also, the YS and ultimate tensile strength (UTS) increase with grain size reduction, which is compatible with the Hall-Petch law. Meanwhile, the strain hardening rate curves match well with the experimental ones in Fig. 4**(b)**. The mechanical curves also reflect a decrease in elongation, which is consistent with the results. This may be related to GBs in the strain hardening [10].

By carefully comparing the model with the experimental results, it is found that the prediction error is less than 5 % when $\varepsilon > 0.10$ in Fig. 5 **(a)**, confirming that the model can predict the stress–strain responses. The errors in stress prediction at low strains are found by combining Figs. 4 and 5**(a)**, which may be associated with the initial deformation behaviour affected by the microstructure [83] and the variation of the dislocation density of mobile dislocations in the grain interior around the macroscopic yield point [10], which are not considered in the present model. Meanwhile, Fig. 5**(b)** clearly indicates the Mises stress cloud for a typical area at $\varepsilon = 0.25$. It can be seen that the model can reflect the stress concentration well. As shown in Fig. 5**(c)**, activated slip or twinning of different grains leads to stress concentration near GBs. Meanwhile, the blocking effect of GBs on slip and twinning results in uneven stress distribution that can be revealed by the model with the CZM for

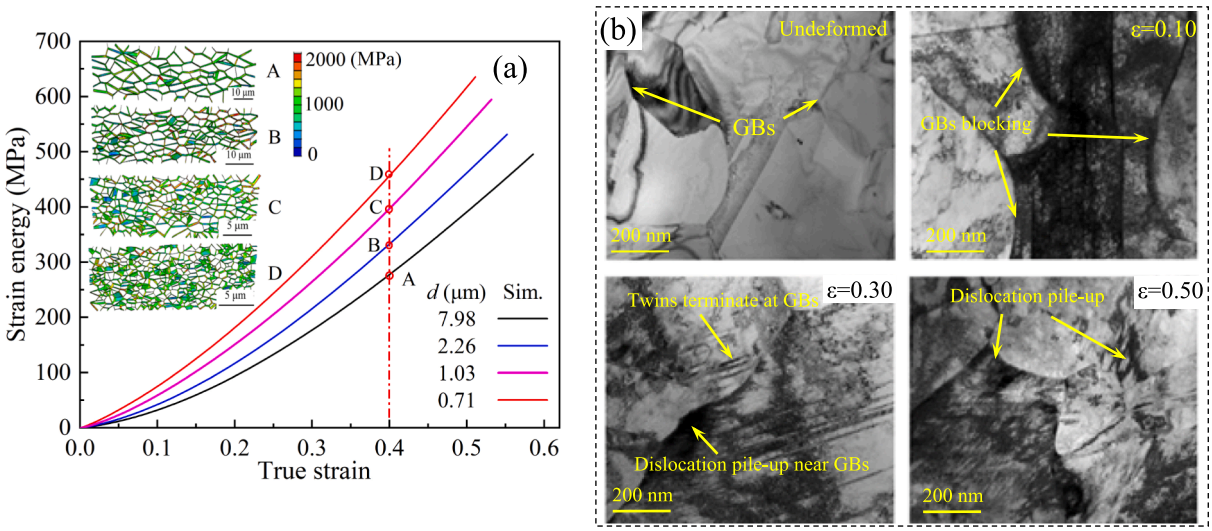

Fig. 9. (a) Evolution of strain energy for GBs networks. (b) BF-TEM images of dislocations and twins blocked by the GBs in strain hardening for specimen with d = 0.70 μ m.

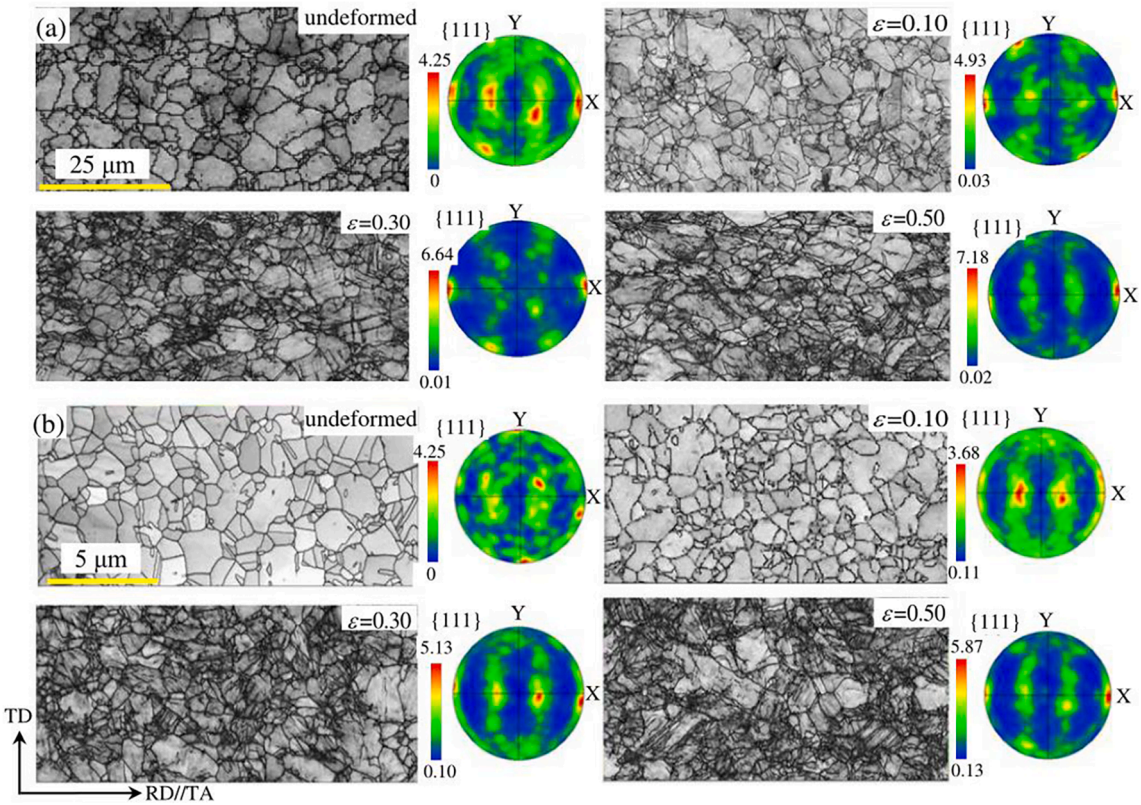

Fig. 10. IQ maps and {111} PFs for the TWIP steel with (a) d = 8.49 μm and (b) d = 0.70 μm at undeformed and the strains of 0.10, 0.30 and 0.50.

GBs. Therefore, the CZM-CPFE method in this work has positive advantages in microstructure evolution.

Fig. 6 indicates the variation of the YS, UTS and uniform elongation (UE) for experimental and simulation results. It can be found that the simulation results can predict the mechanical indicators accurately. Based experimental data, the YS fitting equation is YS = 132.3 + 148.6/$\sqrt{d}$. Also, as the grain size decreases, the UTS for the experiment (E) and simulation (S) increases (K_{UTS-E}=290.9 andK_{UTS-S} = 290.6 MPa·μm$^{0.5}$), while the UE decreases slightly (K_{UE-E}=-0.09, K_{UE-S}=-0.08 μm$^{0.5}$). The former is attributed to the reduction in MFP of dislocations within the grain promoting strain hardening, which is a crucial factor for increasing the strain hardening rate during the initial stage of plastic deformation as the grain size decreases in Fig. 4**(b)**. The reduction of the UE in fine-/ultrafine-grained TWIP steel may be related to the twin suppression and strain localization. In addition, it was found that the fitted correlation coefficients Rc (absolute value) for YS, UTS and UE all exceeded 0.9, indicating that they have a good linear correlation.

4.3.2. Effect of microstructural factors on the evolution of dislocations and deformation twins

The plastic deformation and damage initiation at GBs were observed

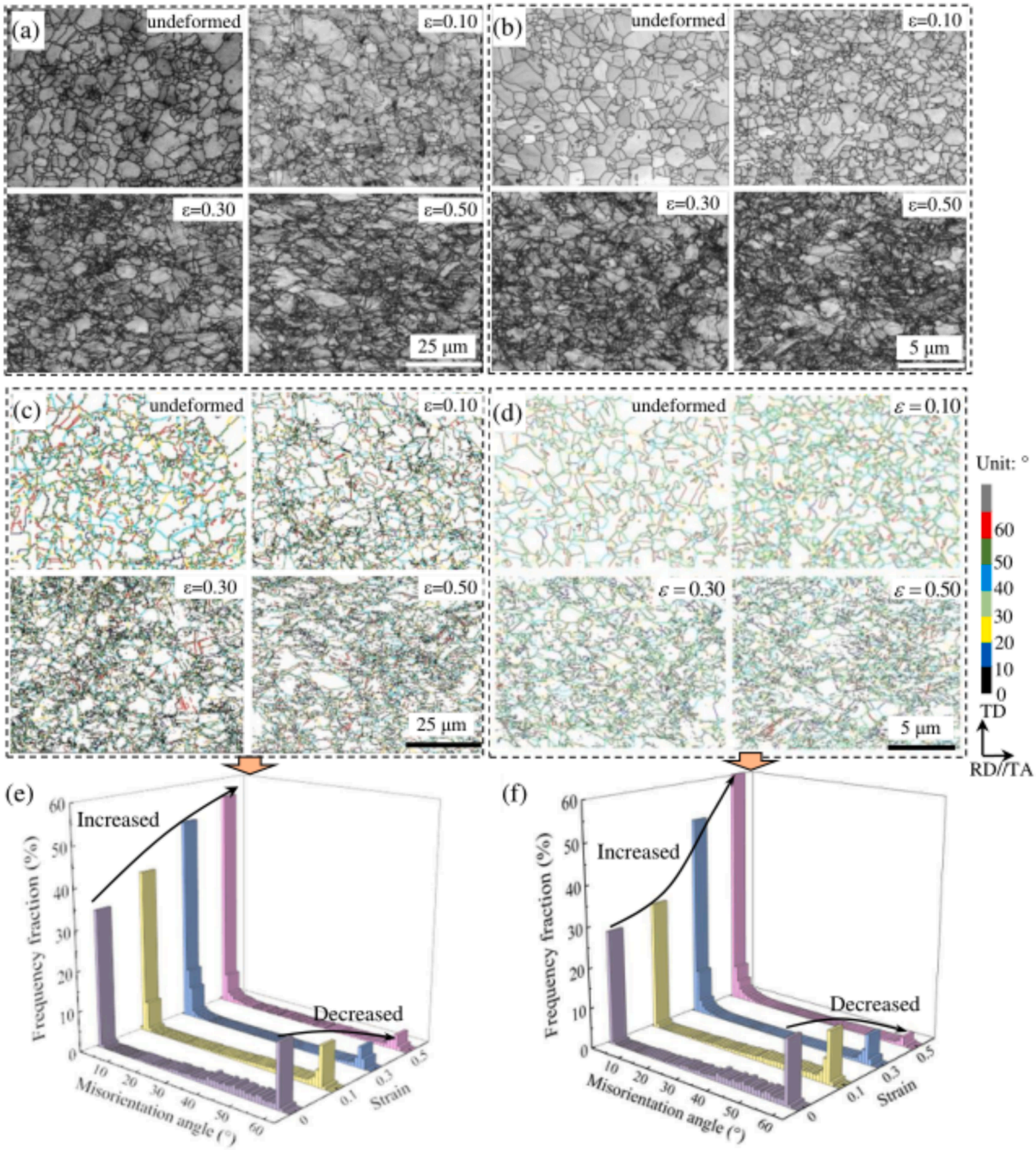

Fig. 11. (a) (b) IQ maps, (c) (d) misorientation angles distribution and (e) (f) statistics of TWIP steel at undeformed and strains of 0.10, 0.30 and 0.50. Where (a)(c)(e) indicates the specimen with $d = 8.49$ μm and (b)(d)(f) indicates the specimen with $d = 0.70$ μm.

based on the in-situ tensile tests for TWIP steels with $d = 8.49$ and 1.01 μm in Fig. 7, where the respective simulation results are also illustrated. It can be noticed that at $\varepsilon = 0.2$, deformation twins and local stress concentrations near GBs appeared in both specimens. The simulation results can reflect the different distributions of stresses. With increasing strain, obvious cracks near GB were observed for the specimen with $d = 8.49$ μm at $\varepsilon = 0.55$ and the specimen with $d = 1.01$ μm at $\varepsilon = 0.45$. They can be predicted by the simulated results of the local higher stresses near the induced cracking GB.

The twin area fraction can be tracked to investigate the microstructural evolution quantitatively. Referring to prior work [66], the evolutions of deformation twins during plastic deformation of TWIP steel with $d = 8.49$ and 0.70 μm were marked based on the IQ-GB maps, as presented in Fig. 8**(a)** and **(b)**, respectively. The twin area fraction was determined based on the number of pixel points in the scanning area. For example, the IQ-GBs map of TWIP steel with $d = 0.70$ μm at $\varepsilon = 0.3$ is presented in Fig. 8**(b)**. The image size is 208 × 104 pixels with a scan step of 0.1 μm, resulting in a detection area of about 20.8 × 10.4 μm^2. Deformation twins were identified and highlighted based on the difference in orientation between the matrix and the twin, {111}-type coherent twin boundaries and lamellar morphological characteristics [84], and they contain 381 pixel points, resulting in an area fraction of 1.76 %. The quantitative evolution of deformation twins for TWIP steel with $d = 8.49$ and 0.70 μm was obtained by the same method.

Meanwhile, the models using the CZM-CPFE method traced the evolution of the twin area fraction to explore the effect of grain refinement on twin evolution. The evolutions of the experimental and simulated twin area fractions are presented in Fig. 8**(c)**. The twin area

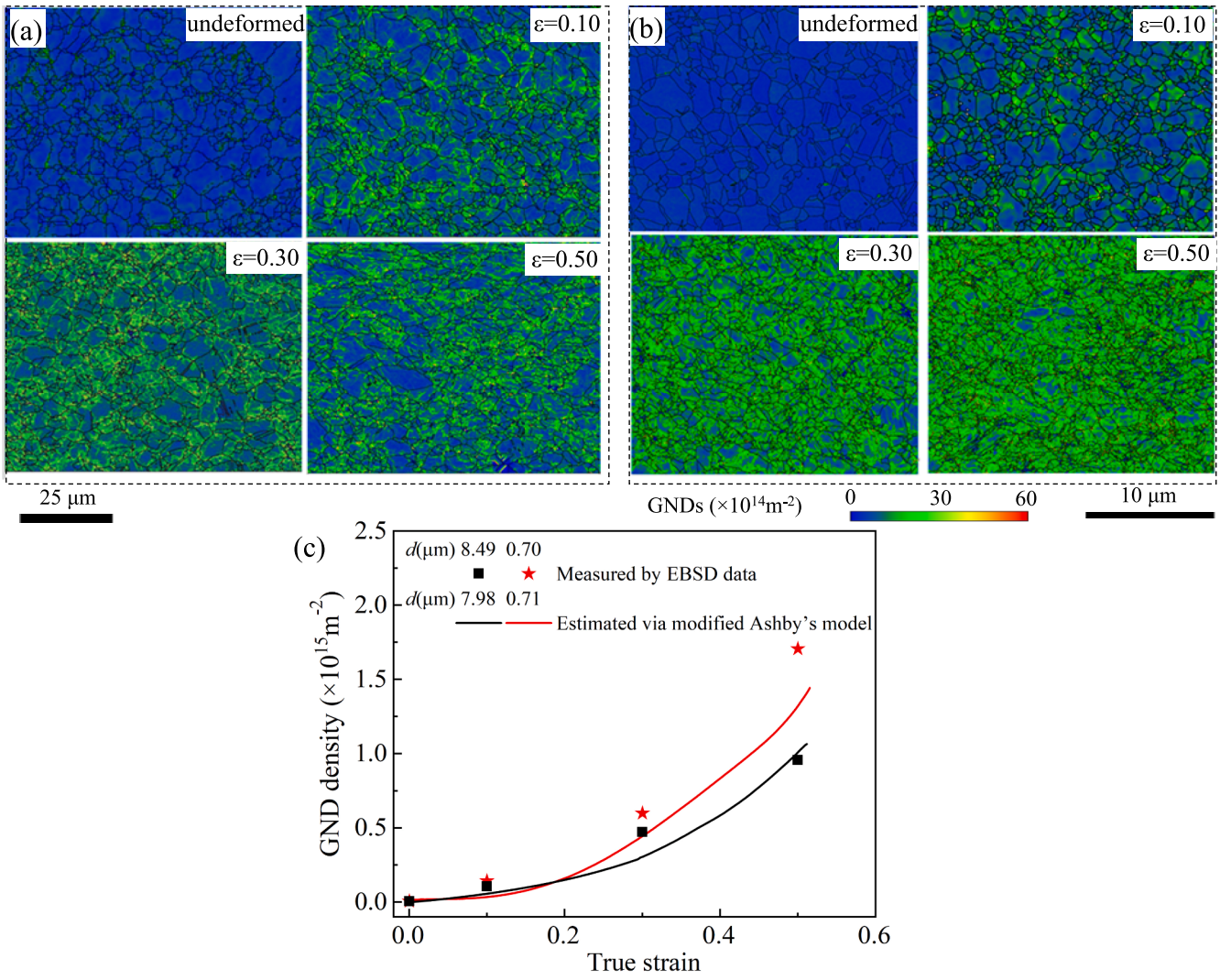

Fig. 12. The evolutions of GND densities for TWIP steel with (a) d = 8.49 and (b) 0.70 μ m, and (c) their experimental statistics and evaluated by the modified Ashby's model at undeformed and the strains of 0.10, 0.30 and 0.50.

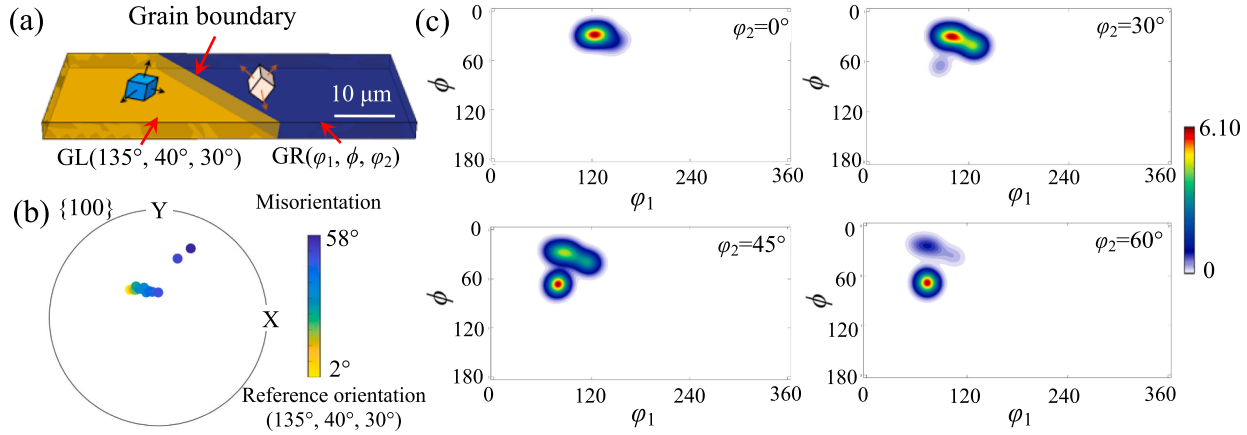

Fig. 13. (a) Model of neighbouring grains consisting of left grain (GL) and right grain (GR). (b) The {100} PF and (c) orientation distribution function (ODF) figures.

fraction decreases with decreasing grain size and the twin area fraction for RVE with d = 0.71 μm is lower than that for other grain sizes at the larger strains, suggesting that the finer grains can inhibit twinning, which may be relevant to the grain refinement that elevates the CRSS for twinning [21], while twinning is inhibited in strain-hardened parent grains, even at higher stress conditions.

Furthermore, to further elaborate on the effect of GBs on strain hardening, the increase in deformation resistance may be associated

Table 4
The maximum Schmid factors (m_{slip} and m_{twin}) for different grain orientations and the corresponding slip system (S) and twinning system (T).

Euler angle of the GL (°)				Slip	Twinning
$\varphi 1$	ϕ	$\varphi 2$	–	m_{slip}/S	m_{twin}/T
135	40	30	–	0.446/S12	0.394/T9
Euler angle of the GR (°)			Slip		Twinning
$\varphi 1$	ϕ	$\varphi 2$	Misorientation (°)	m_{slip}/S	m_{twin}/T
134	41	29	2	0.432/S9	0.398/T12
131	39	29	5	0.435/S9	0.409/T12
129	43	28	8	0.447/S9	0.436/T12
126	42	29	10	0.440/S9	0.438/T12
123	40	26	15	0.446/S9	0.463/T12
115	34	25	25	0.430/S9	0.475/T12
115	29	21	30	0.447/S7	0.489/T12
108	30	21	36	0.468/S7	0.478/T12
103	30	20	42	0.478/S7	0.461/T12
95	30	20	50	0.468/S7	0.420/T10
78	66	48	54	0.418/S3	0.455/T2
72	70	60	58	0.320/S3	0.387/T2

with the densification of the GBs networks except for slip and twinning activation [13]. The energy storage of the GBs tracked using the CZM are shown in Fig. 9**(a)**. As the grain size decreases, the strain energy storage of GBs gradually increases. Grain refinement leads to greater stress that is required for twin nucleation. Thus, the twin is further suppressed. Fig. 9**(b)** illustrates the bright field transmission electron microscopy (BF-TEM) images of the specimens with different strains, where dislocations are found to pile up mainly in one-sided grain near GB, while the thinner twins also terminate at GBs, which indicates the blocking effects of the GBs on the dislocation motion and the growth of thin twins. The reliability of the stress uneven distribution is validated by the embedded CZM in the CPFE model. Thus, the plastic deformation behaviours of TWIP steels with fine and ultrafine grains are influenced by the combined effect of slip, twins and GBs.

The CPFE model can reasonably elaborate the effects of grain size on yield stress and strain hardening. Meanwhile, the CZM is able to illustrate the mechanical characteristics of GBs in terms of the geometrical structure, which is first damaged and cracked during plastic deformation. TEM characterises dislocation pile-up and twin termination near GBs, revealing the blocking effect of GB on dislocation motion and twin growth, which results in stress concentrations near the GBs. The CZM-CPFE method can be employed to predict the evolution of

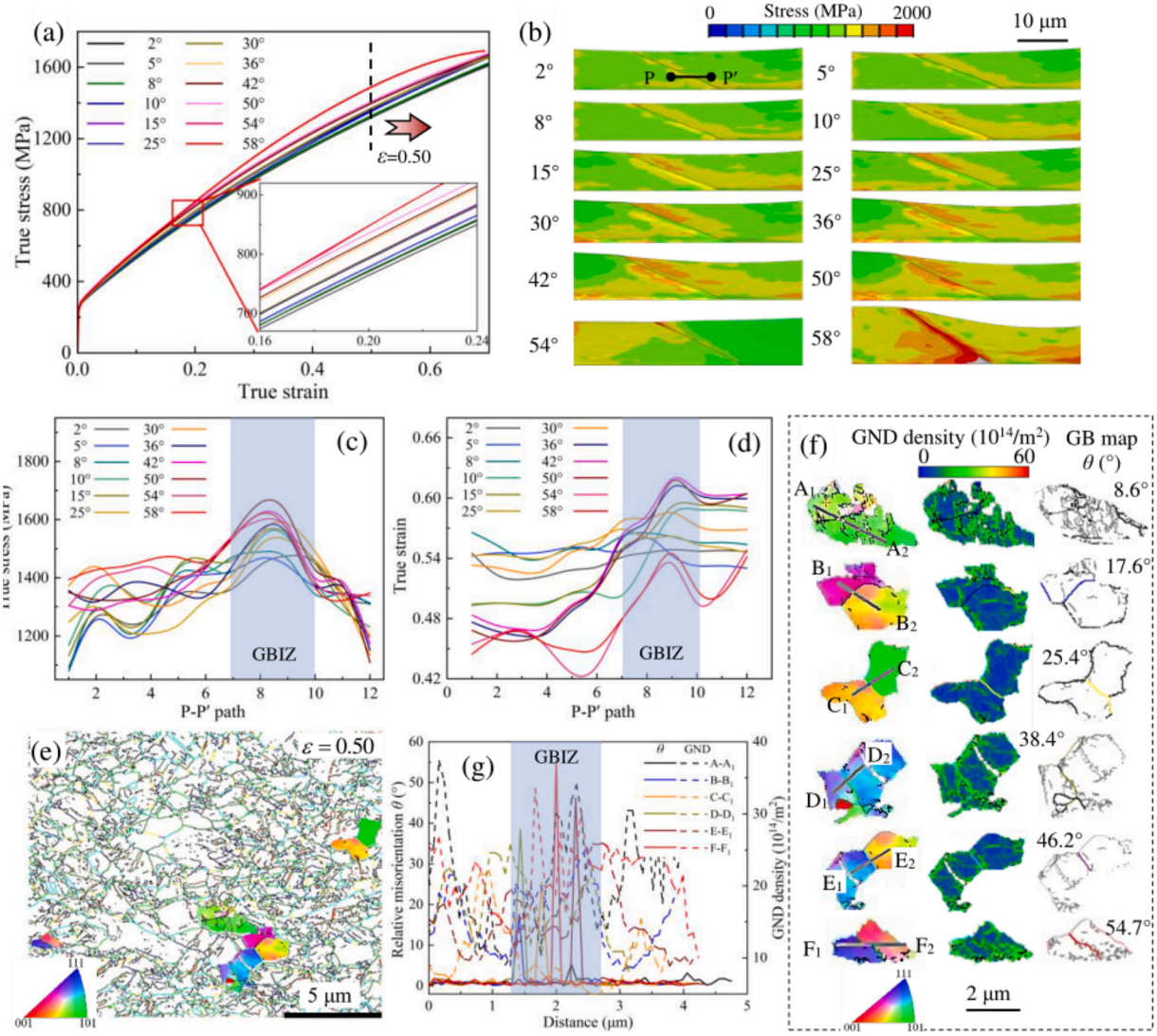

Fig. 14. Simulation of models for two grains with GB modelled by the CZM: (a) stress strain responses and (b) stress distributions for different misorientation angles at $\varepsilon = 0.50$. (c) True stress and (d) strain distributions along the P-P′ path in (b). (e) The GBs network at $\varepsilon = 0.50$, (f) the EBSD-IPFs, GND densities and misorientation maps of grain sets with these marked different misorientation angles, (g) relative misorientation angles along the marked lines direction in (f).

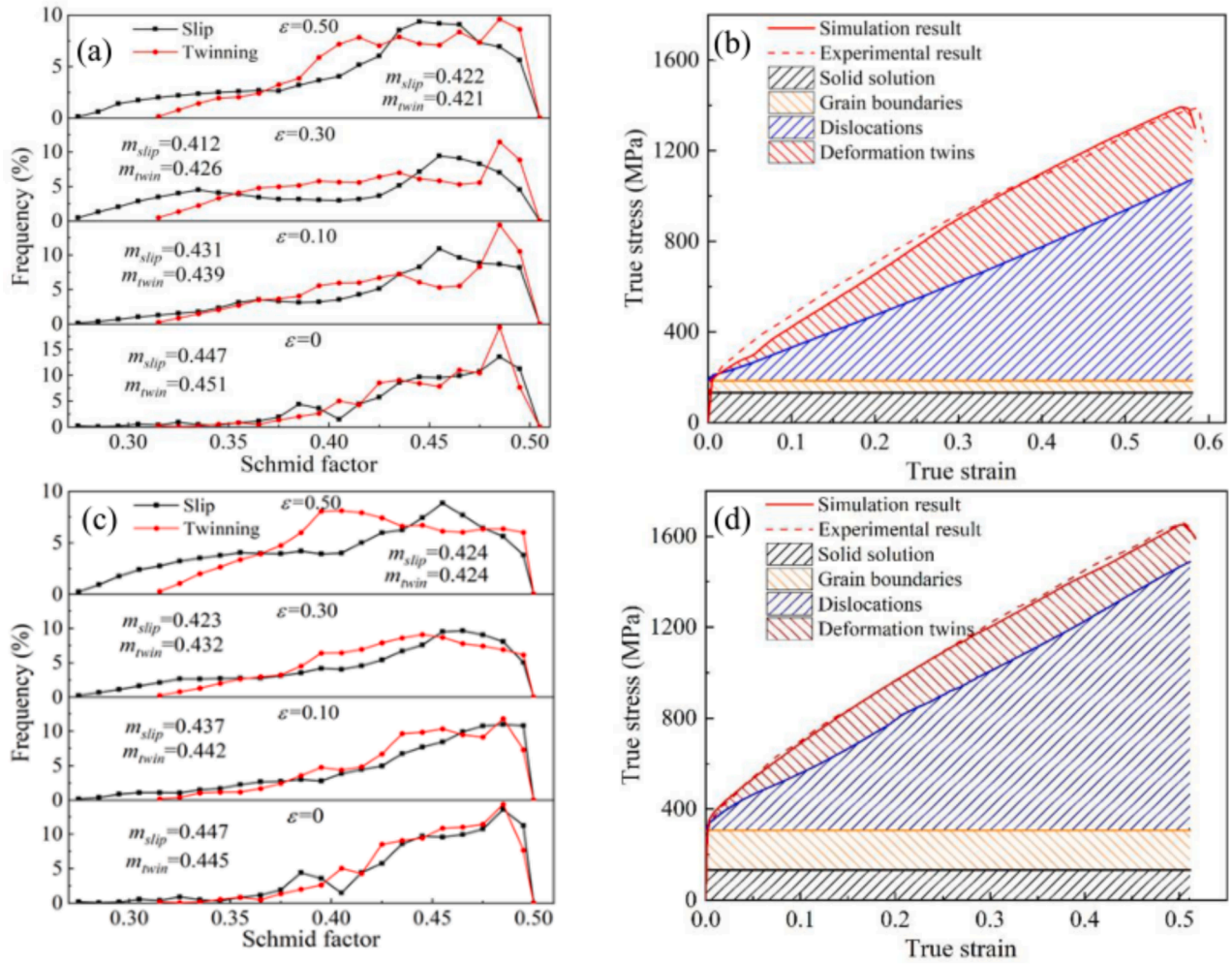

Fig. 15. The m_{slip} and m_{twin} of $\varepsilon = 0$, 0.10, 0.30 and 0.50 for TWIP steels with (a) $d = 8.49$ μm and (c) $d = 0.70$ μm. The respective contributions of solid solution, grain boundaries, dislocations and deformation twins to the true stress during plastic deformation for TWIP steels with (b) $d = 8.49$ μm and (d) $d = 0.70$ μm.

microstructures and mechanical behaviours.

In order to analyse more carefully the effect of plastic deformation on the orientation distribution, Fig. 10 shows the IQ maps at the strain points marked in Fig. 4**(a)**. It can be revealed that dislocations and deformation twins were produced with increasing strain for both TWIP steels with $d = 8.49$ and 0.70 μm, the accumulation of dislocations induced subgrains, which are densely distributed near the GBs in Fig. 10 **(a)** and **(b)**. Also, the grain orientation distributions during plastic deformation are similar for both TWIP steels with different sizes, and no strong textural effects are produced based on the {111} PFs.

It is commonly accepted that there is a balance between strength and ductility in many alloys [26,27], which may be related to misorientation angles and dislocation behaviours [85]. The IQ maps in Fig. 11**(a)** and **(b)** presented the microstructural evolution with increasing strain due to dislocation accumulation and deformation twin formation. The distributions of misorientation angles at different strains of TWIP steel with $d = 8.49$ and $d = 0.70$ μm are presented in Fig. 11**(c)** and **(d)**. The evolutions of misorientation angles with strain are statistically calculated in Fig. 11**(e)** and **(f)**. For the TWIP steel with $d = 8.49$ μm, strain increased to 0.50, the low angle grain boundaries (LAGBs) increased from ~ 30 % to ~ 58 % and the fraction of TBs decreased from ~ 13.8 % to ~ 5.2 %, respectively. While for the TWIP steel with $d = 0.70$ μm, LAGBs increased from ~ 28 % to ~ 61 %, the fraction of TBs decreased from ~ 16 % to ~ 3 %. With increasing strain, twinning, although suppressed, is activated in some grains. Thus, the reduction of TBs fraction is mainly attributed to the formation of dislocation substructures and subgrains.

The evolutions of GND density for TWIP steel with $d = 8.49$ and 0.70 μm are presented in Fig. 12**(a)** and **(b)**, respectively. The higher GND density in Fig. 12**(b)** indicates that grain refinement promotes dislocation activation. Also, to improve computational efficiency and quantify GNDs density based on the model, due to the microstructures in the grain interior such as dislocations and deformation twins, ρ_{GND} needs to be modified by the MFP of dislocations. Based on Eq. (13), Eq. (1) can be modified:

$$\rho_{GND} \cong \frac{\varepsilon_p}{4b}\left(\frac{1}{d}+\frac{\sum_{\beta=1}^{12}B^{\alpha\beta}f^{\beta}}{2re(1-f_t^{\beta})}+\frac{\sum_{\alpha=1}^{12}\sqrt{\sum_{i\neq\alpha}\rho^i}}{12K}\right) \tag{26}$$

Eq. (26) considers the dislocation interactions, dislocation and twin interactions. The GND density is evaluated based on Eq. (26). Fig. 12**(c)** presents the evolutions of GND densities measured in experiments and evaluated by the modified Ashby's model for TWIP steels with $d = 8.49$ and 0.70 μm. The measured ρ_{GND} increases from 1.05×10^{14} m^{-2} to 9.60×10^{14} m^{-2} for specimen with $d = 8.49$ μm and from 1.43×10^{14} m^{-2} to 1.71×10^{15} m^{-2} for specimen with $d = 0.70$ μm when strain increased from 0.10 to 0.50. The modified Ashby's model can estimate the evolution of ρ_{GND}, but the error is about 13 % for specimen with $d = 0.70$ μm at $\varepsilon = 0.50$ due to not considering substructures in the model. In fact, the aggregation of GNDs can promote local lattice rotation, creating favourable conditions for the formation of substructures and subgrains [7]. Also, GBs can be regarded as crucial locations for dislocation

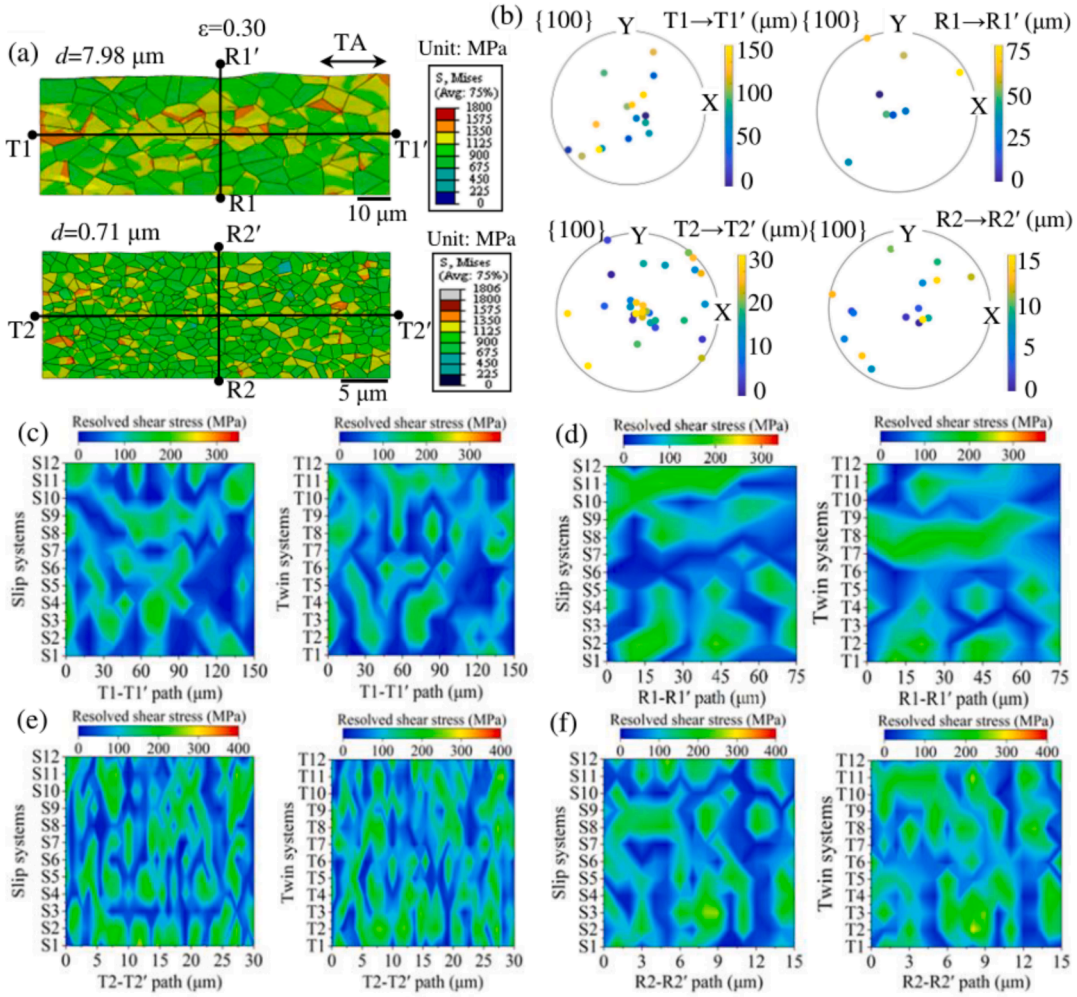

Fig. 16. At $\varepsilon = 0.30$: (a) T1-T1′ and R1-R1′ paths for RVE with $d = 7.98$ μ m, T2-T2′ and R2-R2′ paths for RVE with $d = 0.71$ μ m, (b) the {100} PFs for these grains. The distribution statistics of the RSS for different slip and twin systems along the (c) T1-T1′, (d) R1-R1′ (e) T2-T2′and (f) R2-R2′ paths, respectively.

generation and annihilation [6], which can affect GB-mediated plastic behaviours [86].

4.3.3. Effect of misorientation angle on the mechanical behaviours of neighbouring grains

To further explore the effect of different misorientation angles on the slip and twinning activation of neighbouring grains, the model is constructed to elaborate the mechanical behaviours based on the CPFE approach. As shown in Fig. 13**(a)**, 12 sets of misorientation angles in 2° to 58° are obtained for the model of the two grains containing GB by fixing the Euler angles of left grain (GL) (135°, 40°, 30°) and varying the Euler angles of right grain (GR) in Table 4. Meanwhile, the orientation distribution of these grains in the {100} PF is presented in Fig. 13**(b)**, where the deviation of the pole position is larger with the orientation angle. Also, the orientation distribution function (ODF) figures of these grains with $\varphi_2 = 0°$, 30°, 45° and 60° are obtained in Fig. 13**(c)**.

The Schmid factors (m_{slip} and m_{twin}) along the loading direction are calculated, while the corresponding slip and twin systems are given in Table 4, where the slip (S1-12) and twin systems (T1-12) are elaborated in Appendix B. It is notable that the associated slip and twin systems are the same when the misorientation angle is not changed much, except that m_{slip} and m_{twin} are different, suggesting that the loading stresses required for activation are different. Meanwhile, for misorientation angles of 54° and 58°, m_{twin} is higher than m_{slip}, which confirms that grain orientation can affect slip and twin activation.

To illustrate the effect of grain misorientation on mechanical behaviours, models of neighbouring grains with GB were constructed. The simulated stress–strain responses are presented in Fig. 14**(a)**. The effect of the misorientation angle on yield stress is not significant. To elucidate the intrinsic factors of stress elevation, the stress distribution for different misorientation angles at $\varepsilon = 0.50$ is presented in Fig. 14**(b)**. The stress near the GB increases gradually with increasing misorientation angle, e.g., the stress near the GB with a misorientation angle of 58° is higher compared to other angles. Nevertheless, it can be revealed that the stresses tend to be more concentrated in the model by comparing the stresses on the P-P′ path in Fig. 14**(c)**. Meanwhile, the strains in the P-P′ path are shown in Fig. 14**(d)**, which indicates that the GB also affects the strain distribution in the grain boundary influence zone (GBIZ). Neighbouring grains with different misorientation angles are selected in the EBSD-IPF at $\varepsilon = 0.5$ as presented in Fig. 14**(f)**. Fig. 14**(g)** illustrates the results of the relative misorientation statistics along the marked lines. Neighbouring grains with different misorientation angles (0-60°) near the GB have different effects on the distribution of GND density. The relatively higher GND densities near the HAGBs indicate a greater concentration of stresses and strains, which indirectly confirms the predictive advantages of the numerical simulation results.

5. Discussion and analysis

Grain refinement retards mechanical twins by increasing the RSS despite the existing inactive twins in TWIP steels [21]. However, the slip system with the highest Schmid factor is considered to be the preferred

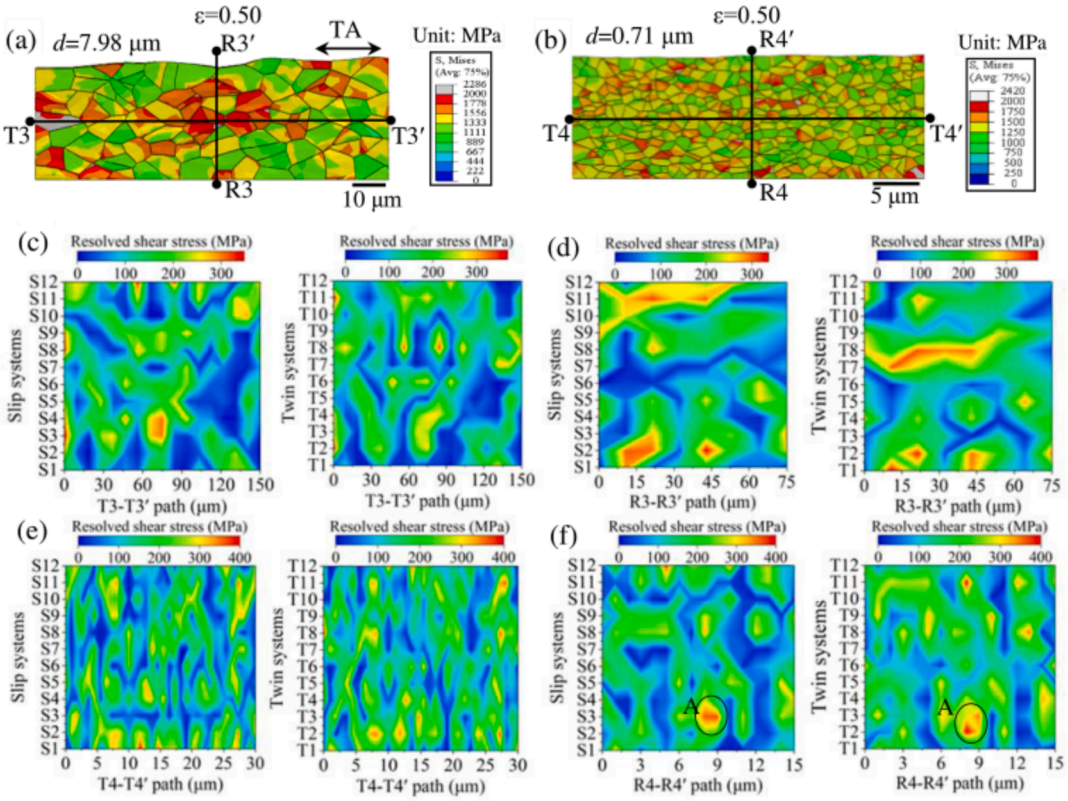

Fig. 17. At $\varepsilon = 0.50$: (a) T3-T3′ and R3-R3′ paths for RVE with $d = 7.98$ μ m, (b) T4-T4′ and R4-R4′ paths for RVE with $d = 0.71$ μ m. The distribution statistics of the RSS for different slip and twin systems along the (c) T3-T3′, (d) R3-R3′ (e) T4-T4′ and (f) R4-R4′ paths, respectively.

activation mode whenever it is possible to select more than one slip mode, which was confirmed in experiments and models [65,87]. Due to the RSS for twinning is higher than that for slip in grains near the < 111>//TA direction, deformation twins are easily activated [21]. To illustrate the contribution of slip and twinning, combining experimental results and previous work [47], the flow stress (σ_{flow}) can be divided into the contributions of solid solution (σ_0), grain boundaries (σ_g), dislocations (σ_{ds}) and deformation twins (σ_T), which is given by the following [47,88]:

$$\sigma_{flow} = \sigma_0 + \sigma_g + \sigma_{ds} + \sigma_T \tag{27}$$

Here, the flow stress involved in the initial slip is related to the YS [89]. It is widely accepted that the dislocation density is quite low and deformation twins are not induced at yielding [73]. Thus, the contribution of solid solution is calculated via $\sigma_0 = \sigma_Y - \sigma_g$, where $\sigma_g = K_{HP}/\sqrt{d}$. The σ_Y is the yield strength, which can be directly obtained based on experimental method. The coefficient $K_{HP} = 148.6$ MPa·μm$^{0.5}$ by fitting and the $d = 0.70$ μm is measured. Also, σ_{ds} is calculated by $\sigma_{ds} = M\alpha\mu b\sqrt{\rho_{tot}}$ [88], where ρ_{tot} is the total dislocation density. Based on the findings [47,88], the σ_T can be calculated by $\sigma_{flow} - \sigma_Y - \sigma_{ds}$. Also, the m_{slip} and m_{twin} with strain evolution for RVEs with $d = 7.98$ and $d = 0.71$ μm are shown in Fig. 15**(a)** and **(c)**. There is a tendency for both m_{slip} and m_{twin} to decrease as the strain increases. According to the description in [87]: $\tau = \sigma \cdot m_s$, where m_s is m_{slip} or m_{twin}, the CRSS for slip $\tau^c_{slip} = 81.7$ MPa for TWIP steel with $d = 8.49$ μm and $\tau^c_{slip} = 138.5$ MPa for TWIP steel with $d = 0.70$ μm are calculated at yielding by the above analysis.

Based on Eq. (20), τ^c_{twin}=190 MPa for TWIP steel with $d = 8.49$ μm and $\tau^c_{twin} = 202$ MPa for TWIP steel with $d = 0.70$ μm are calculated. During the quasi-static loading, the temperature does not change, and thus, the SFE can be considered unaffected. Combined with the evolution of the dislocation density in the CPFE model, the contribution of dislocations to strain hardening can be evaluated. Fig. 15**(b)** and **(d)** present the contributions of solid solution, grain boundaries, dislocations and deformation twins on the true stress for TWIP steel with $d =$ 8.49 and 0.70 μm, respectively, where the solid solution stress (σ_0) and the contribution of GBs (σ_g) are considered constant. In contrast, the contribution of dislocations increases gradually with strain [47,88] and dominates at during all deformation stages. Compared to dislocation, the contribution of deformation twins is relatively small, which is consistent with the findings of Liang et al [88].

To more deeply understand slip and twinning activation, many grains along T1-T1′ and R1-R1′ paths for RVE with $d = 7.98$ μm and T2-T2′ and R2-R2′ paths for RVE with $d = 0.71$ μm at $\varepsilon = 0.30$ are selected in Fig. 16**(a)**, respectively. Fig. 16**(b)** depicts the {100} PFs for these grains along the paths, which reflects a roughly random distribution of grain orientations for both RVEs. m_{slip} and m_{twin} along the TA direction can be calculated based on these orientations. The RSS for the different slip and twin systems are evaluated based on the contributions of dislocation and twin to strain hardening, with the distributions revealed in Fig. 16**(c)**~(f). The resolved shear stresses for slip and twinning vary considerably in different grains and in different slip and twinning systems.

In addition, the resolved shear stresses for slip and twinning along T3-T3′ and R3-R3′ paths for RVE with $d = 7.98$ μm and T4-T4′ and R4-R4′ paths for RVE with $d = 0.71$ μm at $\varepsilon = 0.50$ were calculated, as shown in Fig. 17. As the strain increases to 0.50, the RSS distributions for the slip and twin systems are roughly similar at $\varepsilon = 0.30$. It is noteworthy that under certain orientation conditions, such as the area marked A in Fig. 17**(f)**, the resolved shear stresses are similar for both slip and twinning. Nevertheless, due to the larger CRSS for twinning compared to slip, slip may be preferentially activated here, suggesting that twinning is suppressed, resulting in a rate of increase in the twin area fraction is flat and the contribution to true stress does not increase dramatically. On the other hand, based on the references [1,89], the CRSS for slip is generally less than that for twinning. Thus, dislocations become the main deformation mechanism. This is consistent with the fact that few

deformation twins were experimentally detected in Fig. 8.

The reduction in grain size elevates the CRSS for slip and twinning, and the subsequent deformation behaviours can be well predicted by the CPFE model, which facilitates a more in-depth, detailed and comprehensive analysis of the plastic deformation for TWIP steels. The micromechanical behaviours of TWIP steel are analysed to illustrate that the tensile properties are associated with the grain size, strain energy, and activation and evolution of slip and twinning affected by shear stresses. Furthermore, the misorientation angle can also influence the slip and twinning during strain hardening [90], which may provide an essential basis for future work.

6. Conclusions

In this work, a CZM-CPFE method was developed to explore the plastic deformation behaviours of TWIP steel. Its reliability and accuracy are confirmed by in-situ SEM tensile tests and EBSD/TEM characterisation of specimens after tensile deformation. Then, the effect of GB with different misorientation angles on the mechanical properties of neighbouring grains was explored. Also, the contributions of dislocation and twinning in the strain hardening for fine- and ultrafine-grained TWIP steels were evaluated by theoretical analysis and simulations. The crucial findings are summarized:

(1) The average grain size of TWIP steel was refined from 8.49 to 0.70 μm by combining the rolling and heat treatment processes. The experimental results illustrated that grain refinement elevated the YS and UTS, which was intimately related to dislocation-dominated plasticity while twinning suppressed. The evolution of the GND density of TWIP steel with $d = 8.49$ and 0.70 μm was characterised using EBSD, which can be evaluated by the modified Ashby's model that considered the effects of dislocations and twins.

(2) The CZM-CPFE approach was developed, where the CPFE model considered the effects of grain size on the stress, dislocation density, and CRSS for slip and twinning, and the CZM was employed to elucidate the mechanical properties of GBs. This approach was employed to analyse the effect of dislocations, twins and grain boundaries on strain hardening, which provided a strategy for predicting mechanically relevant behaviours such as yielding and subsequent strain hardening of TWIP steel with moderate grain sizes. Furthermore, the simulation results of the neighbouring grain model corroborated that the increase of the misorientation angle promoted the stress concentration near GBs.

(3) Detailed quantitative calculations of macroscopic flow stresses revealed the dislocation is dominant during all deformation stages. In contrast, the contribution of deformation twins is small and not significantly increased at large strains. Based on the experimental results and calculations, it was indicated that the grain refinement enhanced the CRSS for slip and twinning and regulated the activation and evolution of dislocations and twins. Also, the results indicated that the excellent mechanical properties are attributed to the combined influences of the strain energy and various microstructural factors such as grain size, deformation twin and dislocation.

CRediT authorship contribution statement

Wang Cai: Writing – review & editing, Visualization, Software, Methodology, Investigation, Data curation, Conceptualization. **Chaoyang Sun:** Writing – review & editing, Supervision, Resources, Project administration, Methodology, Funding acquisition. **Hongjia Zhang:** Methodology, Investigation, Data curation. **Lingyun Qian:** Funding acquisition, Methodology, Writing – review & editing. **Linghui Meng:** Writing – review & editing, Software. **M.W. Fu:** Writing – review & editing, Supervision, Methodology, Funding acquisition.

Declaration of competing interest

The authors declare that they have no known competing financial interests or personal relationships that could have appeared to influence the work reported in this paper.

Acknowledgements

The authors acknowledge the funding supported by the National Natural Science Foundation of China (No. 52275305, 52175285, U22A20186), and the projects of G-SB4Y, 1-ZE1W, 1-CD4H, and H-ZGDV from the Hong Kong Polytechnic University and the projects 15228621, 15229922 and C4074-22G from General Research Fund of Hong Kong Government.

Appendix A:. Interaction of TWIP steel slip systems

In order to distinguish the different slip systems of TWIP steels, six possible types of interactions between slip systems were identified among the 12 slip systems in FCC structure [30,65], including self-hardening (A_0), coplanar (A_1), co-linear (A_2), orthogonal (A_3), glissile (A_4) and sessile (A_5) types [57]. In this work, the symmetry of FCC structure is noted, so that the interaction matrix $A_{\alpha\alpha'}$ in Eq. (9) is expressed by the following:

$$A_{\alpha\alpha'} = \begin{bmatrix} A_0 & A_1 & A_1 & A_2 & A_4 & A_4 & A_3 & A_4 & A_3 & A_3 & A_5 & A_4 \\ A_1 & A_0 & A_1 & A_4 & A_3 & A_5 & A_4 & A_2 & A_4 & A_5 & A_3 & A_4 \\ A_1 & A_1 & A_0 & A_4 & A_5 & A_3 & A_3 & A_4 & A_3 & A_4 & A_4 & A_2 \\ A_2 & A_4 & A_4 & A_0 & A_1 & A_1 & A_3 & A_5 & A_4 & A_3 & A_4 & A_5 \\ A_4 & A_3 & A_5 & A_1 & A_0 & A_1 & A_5 & A_3 & A_4 & A_4 & A_2 & A_4 \\ A_4 & A_5 & A_3 & A_1 & A_1 & A_0 & A_4 & A_4 & A_2 & A_5 & A_4 & A_3 \\ A_3 & A_4 & A_3 & A_3 & A_5 & A_4 & A_0 & A_1 & A_1 & A_2 & A_4 & A_4 \\ A_4 & A_2 & A_4 & A_5 & A_3 & A_4 & A_1 & A_0 & A_1 & A_4 & A_3 & A_5 \\ A_3 & A_4 & A_3 & A_4 & A_4 & A_2 & A_1 & A_1 & A_0 & A_4 & A_5 & A_3 \\ A_3 & A_5 & A_4 & A_3 & A_4 & A_5 & A_2 & A_4 & A_4 & A_0 & A_1 & A_1 \\ A_5 & A_3 & A_4 & A_4 & A_2 & A_4 & A_4 & A_3 & A_5 & A_1 & A_0 & A_1 \\ A_4 & A_4 & A_2 & A_5 & A_4 & A_3 & A_4 & A_5 & A_3 & A_1 & A_1 & A_0 \end{bmatrix} \tag{A1}$$

Table A1
Interaction coefficient values of TWIP steel slip systems [8].

A_0	A_1	A_2	A_3	A_4	A_5
0.122	0.122	0.625	0.07	0.137	0.127

Appendix B:. The slip and twin systems of TWIP steels

.

Table B1
The slip systems of TWIP steel in this work.

No.	Slip plane	Slip direction	No.	Slip plane	Slip direction
S1	(1 1 1)	[0—1 1]	S7	(1—1 1)	[0 1 1]
S2	(1 1 1)	[1 0—1]	S8	(1—1 1)	[1 1 0]
S3	(1 1 1)	[-1 1 0]	S9	(1—1 1)	[1 0—1]
S4	(−1 1 1)	[1 0 1]	S10	(1 1—1)	[0 1 1]
S5	(−1 1 1)	[1 1 0]	S11	(1 1—1)	[1 0 1]
S6	(−1 1 1)	[0—1 1]	S12	(1 1—1)	[-1 1 0]

Table B2
The twin systems of TWIP steel in this work.

No.	Twin plane	Twin direction	No.	Twin plane	Twin direction
T1	(1 1 1)	[1 1—2]	T7	(−1—1 1)	[1 1 2]
T2	(1 1 1)	[-2 1 1]	T8	(−1—1 1)	[2 –11]
T3	(1 1 1)	[1 –21]	T9	(−1—1 1)	[-1 2 1]
T4	(−1 1 1)	[2 1 1]	T10	(1—1 1)	[1 2 1]
T5	(−1 1 1)	[12 –1]	T11	(1—1 1)	[2 1—1]
T6	(−1 1 1)	[1 –12]	T12	(1—1 1)	[-1 1 2]

Data availability

Data will be made available on request.

References

[1] B.C. De Cooman, Y. Estrin, S.K. Kim, Acta Mater. 142 (2018) 283–362.
[2] Gao, B., Lai, Q., Cao, Y., Hu, R., Xiao, L., Pan, Z., Liang, N., Li, Y., Sha, G., Liu, M. Science advances 6 (2020) eaba8169.
[3] I.B. Timokhina, A. Medvedev, R. Lapovok, Mater. Sci. Eng. A 593 (2014) 163–169.
[4] J.G. Kim, N.A. Enikeev, M.M. Abramova, B.H. Park, R.Z. Valiev, H.S. Kim, Mater. Sci. Eng. A 682 (2017) 164–167.
[5] R. Ueji, N. Tsuchida, D. Terada, N. Tsuji, Y. Tanaka, A. Takemura, K. Kunishige, Scripta Mater. 59 (2008) 963–966.
[6] S. Kang, J.G. Jung, M. Kang, W. Woo, Y.K. Lee, Mater. Sci. Eng. A 652 (2016) 212–220.
[7] C. Lei, X. Deng, X. Li, Z. Wang, Scripta Mater. 162 (2019) 421–425.
[8] X. Lu, X. Zhang, M. Shi, F. Roters, G. Kang, D. Raabe, Int. J. Plast. 113 (2019) 52–73.
[9] A.S. Khan, J. Liu, Int. J. Plast. 86 (2016) 56–69.
[10] C.Y. Hung, Y. Bai, N. Tsuji, M. Murayama, J. Mater. Sci. Technol. 86 (2021) 192–203.
[11] C.Y. Hung, T. Shimokawa, Y. Bai, N. Tsuji, M. Murayama, Sci. Rep. 11 (2021) 1–13.
[12] C.Y. Sun, N. Guo, M.W. Fu, S.W. Wang, Int. J. Plast. 76 (2016) 186–212.
[13] W. Cai, C. Sun, C. Wang, L. Qian, Y. Li, M.W. Fu, Int. J. Plast. 156 (2022) 103366.
[14] A.A. Saleh, E.V. Pereloma, A.A. Gazder, Acta Mater. 61 (7) (2013) 2671–2691.
[15] S.J. McCormack, W. Wen, E.V. Pereloma, C.N. Tomé, A.A. Gazder, A.A. Saleh, Acta Mater. 156 (2018) 172–182.
[16] H. Zhi, S. Antonov, C. Zhang, Z. Guo, Y. Su, Mater. Sci. Eng. A 792 (2020) 139834.
[17] H. Yu, C. Li, Y. Xin, A. Chapuis, X. Huang, Q. Liu, Acta Mater. 128 (2017) 313–326.
[18] S. Haouala, S. Lucarini, J. Llorca, J. Segurado, J. Mech. Phys. Solids 134 (2020) 103755.
[19] A. Abdul-Latif, A. Kerkour-El Miad, R. Baleh, H. Garmestani, Mech. Mater. 126 (2018) 1–12.
[20] Y. Wang, C. Huang, X. Ma, J. Zhao, F. Guo, X. Fang, Y. Zhu, Y. Wei, Int. J. Plast. 164 (2023) 103574.
[21] I. Gutierrez-Urrutia, S. Zaefferer, D. Raabe, Mater. Sci. Eng. A 527 (2010) 3552–3560.
[22] K.M. Rahman, V.A. Vorontsov, D. Dye, Acta Mater. 89 (2015) 247–257.
[23] X. Lu, J. Zhao, Z. Wang, B. Gan, J. Zhao, G. Kang, X. Zhang, Int. J. Plast. 130 (2020) 102703.
[24] D.T. Pierce, J.A. Jiménez, J. Bentley, D. Raabe, C. Oskay, J.E. Wittig, Acta Mater. 68 (2014) 238–253.
[25] Y.T. Zhu, X.Z. Liao, X.L. Wu, J. Narayan, J. Mater. Sci. 48 (2013) 4467–4475.
[26] Y. Bai, H. Kitamura, S. Gao, Y. Tian, N. Park, M.H. Park, H. Adachi, A. Shibata, M. Sato, M. Murayama, N. Tsuji, Sci. Rep. 11 (2021) 1–15.
[27] J.Y. Lee, J.S. Hong, S.H. Kang, Y.K. Lee, Mater. Sci. Eng. A 809 (2021) 140972.
[28] A. Lakshmanan, M. Yaghoobi, K.S. Stopka, V.J. Sundararaghavan, Mater. Res. Technol. 19 (2022) 3337–3354.
[29] D. Agius, A. Kareer, A.A. Mamun, C. Truman, D.M. Collins, M. Mostafavi, D. Knowles, Int. J. Plast. 152 (2022) 103249.
[30] S. Haouala, J. Segurado, J. Llorca, Acta Mater. 148 (2018) 72–85.
[31] Y. Zhang, X. Zhang, J. Wang, X. Ren, X. Wang, R. Chen, Z. Yue, Int. J. Plast. 162 (2023) 103526.
[32] J. Chen, J. Lu, W. Cai, Y. Zhang, Y. Wang, W. Jiang, M. Rizwan, Z. Zhang, Int. J. Plast. 163 (2023) 103554.
[33] M. Jiang, Z. Fan, S. Kruch, B. Devincre, Int. J. Plast. 150 (2022) 103181.
[34] E. Alabort, D. Barba, S. Sulzer, M. Lißner, N. Petrinic, R.C. Reed, Acta Mater. 151 (2018) 377–394.
[35] P. Zhang, M. Karimpour, D. Balint, J. Lin, Int. J. Numer. Eng. 92 (8) (2012) 715–733.
[36] R. Quey, P.R. Dawson, F. Barbe, Comput. Method. Appl. M. 200 (17–20) (2011) 1729–1745.
[37] H. Li, D. Huang, M. Zhan, Y. Li, X. Wang, S. Chen, Comp. Mater. Sci. 140 (2017) 159–170.
[38] L.Y. Liu, Q.S. Yang, X. Liu, X.C. Nian, Eng. Fract. Mech. 242 (2021) 107507.
[39] P.F. Gao, M.Y. Fei, M. Zhan, M.W. Fu, Int. J. Plast. 165 (2023) 103609.
[40] Carlsson, K. Master's thesis. Chalmers University of Technology, 2013.
[41] B. Ahmadikia, L. Wang, M.A. Kumar, I.J. Beyerlein, Acta Mater. 244 (2023) 118556.
[42] R. Mohammadzadeh, Mater. Sci. Eng. A 782 (2020) 139251.
[43] E. Bayerschen, A.T. McBride, B.D. Reddy, T.J. Böhlke, Mater. Sci. 51 (2016) 2243–2258.
[44] Y. Zhao, Q. Song, H. Ji, W. Cai, Z. Liu, Y. Cai, Mater. Design 221 (2022) 110998.
[45] X.F. Tang, L.F. Peng, S.Q. Shi, M.W. Fu, Int. J. Plast. 118 (2019) 147–172.
[46] Y. Jia, S. Jiang, J. Tan, Z. Lu, J. Jiang, X. Wang, Acta Mater. 222 (2022) 117452.
[47] H. Zhi, C. Zhang, S. Antonov, H. Yu, T. Guo, Y. Su, Acta Mater. 195 (2020) 371–382.
[48] M. Ashby, Philos. Mag. 21 (1970) 399–424.
[49] C. Zhu, T. Harrington, G.T. Gray III, K.S. Vecchio, Acta Mater. 155 (2018) 104–116.

[50] S.R. Kalidindi, Int. J. Plast. 17 (2001) 837–860.
[51] A.A. Salem, S.R. Kalidindi, S.L. Semiatin, Acta Mater. 53 (2005) 3495–3502.
[52] X. Shang, Z. Cui, M.W. Fu, Int. J. Mech. Sci. 144 (2018) 800–812.
[53] X. Shang, Z. Cui, M.W. Fu, Int. J. Plast. 95 (2017) 105–122.
[54] X. Tong, Y. Li, M.W. Fu, Int. J. Mech. Sci. 267 (2024) 108971.
[55] U.F. Kocks, H. Mecking, Prog. Mater. Sci. 48 (3) (2003) 171–273.
[56] Z.Y. Feng, H. Li, D. Zhang, X.X. Guo, Y.Q. Chen, M.W. Fu, Int. J. Plast. 156 (2022) 103364.
[57] L. Kubin, B. Devincre, T. Hoc, Acta Mater. 56 (2008) 6040–6049.
[58] M.I. Latypov, S. Shin, B.C. De Cooman, H.S. Kim, Acta Mater. 108 (2016) 219–228.
[59] H. Mecking, U. Kocks, Acta Metall. 29 (1981) 1865–1875.
[60] D.R. Steinmetz, T. Jäpel, B. Wietbrock, P. Eisenlohr, I. Gutierrez-Urrutia, A. Saeed-Akbari, T. Hickel, F. Roters, D. Raabe, Acta Mater. 61 (2013) 494–510.
[61] S. Allain, J.P. Chateau, O. Bouaziz, Mater. Sci. Eng. A 387–389 (2004) 143–147.
[62] B. Devincre, T. Hoc, L. Kubin, Science 320 (2008) 1745–1748.
[63] M. Shiekhelsouk, V. Favier, K. Inal, M. Cherkaoui, Int. J. Plast. 25 (2009) 105–133.
[64] M.G. Moghaddam, A. Achuthan, B.A. Bednarcyk, S.M. Arnold, E.J. Pineda, Mater. Sci. Eng. A 703 (2017) 521–532.
[65] Z.X. Su, N. Li, C.Y. Sun, J.Q. Zhao, C.H. Wang, L.Y. Qian, Mater. Sci. Technol. 35 (12) (2019) 1436–1447.
[66] M. Madivala, A. Schwedt, S.L. Wong, F. Roters, U. Prahl, W. Bleck, Int. J. Plast. 104 (2018) 80–103.
[67] C. Wang, C. Sun, L. Qian, W. Cai, J. Jiang, Y. Xiao, Mater. Sci. Tech. 37 (2021) 280–291.
[68] Y.F. Shen, N. Jia, Y.D. Wang, X. Sun, L. Zuo, D. Raabe, Acta Mater. 97 (2015) 305–315.
[69] S. Curtze, V.T. Kuokkala, Acta Mater. 58 (2010) 5129–5141.
[70] J. Gao, S. Jiang, H. Zhang, Y. Huang, D. Guan, Y. Xu, S. Guan, L.A. Bendersky, A. V. Davydov, Y. Wu, H. Zhu, Y. Wang, Z. Lu, W.M. Rainforth, Nature 590 (2021) 262–267.
[71] T. Yalçinkaya, İ. Özdemir, I. Simonovski, Int. J. Mater. Form. 11 (2017) 729–741.
[72] H. Long, L. Liang, Y. Wei, Int. J. Solids Struct. 163 (2019) 194–210.
[73] W. Cai, C. Sun, H. Zhang, C. Wang, L. Meng, M.W. Fu, Mater. Charact. 210 (2024) 113780.
[74] C. Wang, W. Cai, C. Sun, X. Li, L. Qian, J. Jiang, Mater. Sci. Eng. A 835 (2022) 142673.
[75] W. Cai, C. Wang, C. Sun, L. Qian, M.W. Fu, Mater. Sci. Eng. A 851 (2022) 143657.
[76] J. Li, B. Lu, Y. Zhang, H. Zhou, G. Hu, R. Xia, Mater. Chem. Phys. 241 (2020) 122391.
[77] X. Zhang, J. Zhao, G. Kang, M. Zaiser, Int. J. Plast. 163 (2023) 103553.
[78] I. Simonovski, L. Cizelj, Eng. Fract. Mech. 110 (2013) 364–377.
[79] S. El Shawish, L. Cizelj, I. Simonovski, Nucl. Eng. Design 261 (2013) 371–381.
[80] A.H. Chokshi, Adv. Eng. Mater. 22 (1) (2020) 1900748.
[81] T. Gebhardt, D. Music, D. Kossmann, M. Ekholm, I.A. Abrikosov, L. Vitos, J. M. Schneider, Acta Mater. 59 (2011) 3145–3155.
[82] H. Lim, S. Subedi, D.T. Fullwood, B.L. Adams, R.H. Wagoner, Mater. Trans. 55 (2014) 35–38.
[83] J. Punyafu, S. Hwang, S. Ihara, H. Saito, N. Tsuji, M. Murayama, Mater. Sci. Eng. A 862 (2023) 144506.
[84] N. Bozzolo, M. Bernacki, Metall. Mater. Trans. A 51 (6) (2020) 2665–2684.
[85] L. Peng, Z. Xu, Z. Gao, M.W. Fu, Int. J. Mech. Sci. 138 (2018) 74–85.
[86] J.P. Liebig, M. Mackovic, E. Spiecker, M. Göken, B. Merle, Acta Mater. 215 (2021) 117079.
[87] B. Guan, Y. Xin, X. Huang, C. Liu, P. Wu, Q. Liu, Int. J. Plast. 153 (2022) 103276.
[88] Z.Y. Liang, Y.Z. Li, M.X. Huang, Scripta Mater. (2016) 28–31.
[89] K. Li, B. Yu, R.D.K. Misra, G. Han, Y.T. Tsai, C.W. Shao, C.J. Shang, J.R. Yang, Z. F. Zhang, Mater. Sci. Eng. A 742 (2019) 116–123.
[90] T.R. Bieler, R. Alizadeh, M. Peña-Ortega, J. Llorca, Int. J. Plast. (2019) 269–290.